Research Square

Preprints are preliminary reports that have not undergone peer review.
They should not be considered conclusive, used to inform clinical practice,
or referenced by the media as validated information.

Multi-omic profiling and machine learning reveal diagnostic metabolic signatures and distinct decidual cellular states in tubal pregnancy and spontaneous abortion

Letong Huang

huangltgzyfk@163.com

Guangzhou University of Chinese Medicine https://orcid.org/0009-0001-5434-4779

Yinghua Yin

Guangzhou University of Chinese Medicine

Yanxi Huang

Guangzhou University of Traditional Chinese Medicine First Affiliated Hospital

Lilin Yang

Guangzhou University of Traditional Chinese Medicine First Affiliated Hospital

Xiaojing Liu

Guangzhou University of Traditional Chinese Medicine First Affiliated Hospital

Xiaozhen Wu

Guangzhou University of Traditional Chinese Medicine First Affiliated Hospital

Jinfeng He

Guangzhou University of Traditional Chinese Medicine First Affiliated Hospital

Kaiwei Li

Guangzhou University of Chinese Medicine

Xuge Huang

Guangzhou University of Traditional Chinese Medicine First Affiliated Hospital

Yuanqi Liang

Guangzhou University of Chinese Medicine

Ziyan Liu

Guangzhou University of Chinese Medicine

Xin Ru Kelly Leow

Guangzhou University of Chinese Medicine

Yingxuan Zhang

Guangzhou University of Traditional Chinese Medicine First Affiliated Hospital

Jie Gao

Guangzhou University of Traditional Chinese Medicine First Affiliated Hospital

Zhuoliang Liu
Guangzhou University of Traditional Chinese Medicine First Affiliated Hospital

Research Article

Keywords: Tubal pregnancy, Spontaneous abortion, serum metabolomics, machine learning, single-cell transcriptomics

Posted Date: October 27th, 2026

DOI: https://doi.org/10.21203/rs.3.rs-11191056/v1

License: This work is licensed under a Creative Commons Attribution 4.0 International License.
Read Full License

Multi-omic profiling and machine learning reveal diagnostic metabolic signatures and distinct decidual cellular states in tubal pregnancy and spontaneous abortion

Letong Huang[1,2*], Yinghua Yin[1,2*], Yanxi Huang[3,4], Lilin Yang[3,4], Xiaojing Liu[3,4], Xiaozhen Wu[3,4], Jinfeng He[3,4],Kaiwei Li[1,2], Xuge Huang[1,2], Yuanqi Liang[1,2], Ziyan Liu[1,2], Xin Ru Kelly Leow[1,2], Yingxuan Zhang[3,4†], Jie Gao[3,4,5†],Zhuoliang Liu [3,4†]

1 First School of Clinical Medicine, Guangzhou University of Chinese Medicine, Guangzhou, China

2 Lingnan Medical Research Center of Guangzhou University of Chinese Medicine, Guangzhou, Guangdong, China

3 Department of Gynecology, The First Affiliated Hospital of Guangzhou University of Chinese Medicine, Guangzhou, Guangdong China

4 Guangdong Clinical Research Academy of Chinese Medicine, Guangzhou, China.

5 State Key Laboratory of Traditional Chinese Medicine Syndrome, Guangzhou, China.

Corresponding author: Yingxuan Zhang, Jie Gao, Zhuoliang Liu

E-mail addresses: zhangyingxuan92720@gzucm.edu.cn (Yingxuan Zhang), gaojie1769@gzucm.edu.cn (Jie Gao), tywzlzl2011@yeah.net (Zhuoliang Liu)

Abstract

Background: Tubal pregnancy (TP) and spontaneous abortion (SA) are prevalent early pregnancy complications that severely compromise gestational safety. Accurate differentiation between normal intrauterine pregnancy (NP), TP and SA at early gestational stages is critical for standardized clinical management and the reduction of adverse pregnancy outcomes. Clinically, intrauterine pregnancy (IUP) includes both normal viable intrauterine pregnancy and non-viable intrauterine pregnancy such as early spontaneous abortion, which serves as the main

control cohort for distinguishing ectopic gestation. Traditional diagnostic approaches relying on serial β-hCG detection and transvaginal ultrasound exhibit limited accuracy for both pregnancy localization and embryonic viability assessment, easily resulting in delayed or inappropriate clinical intervention for TP and SA patients.

Methods: Untargeted serum metabolomics based on UHPLC-MS/MS was performed on serum samples from 50 patients with TP, 50 patients with SA and 50 individuals with uncomplicated NP. Multivariate statistical analyses and KEGG pathway enrichment were used to screen differential metabolites and characterize disease-specific metabolic perturbations. Samples were randomly allocated to a training set comprising 60% of the cohort and a validation set comprising the remaining 40%. Diagnostic models for pregnancy localization discrimination and embryonic viability assessment were established, with model efficacy verified via multiple indicators and core predictive metabolites screened through SHAP analysis. Furthermore, scRNA-seq of decidual tissues from TP, SA and NP patients was performed to decipher the cellular and molecular mechanisms underlying disease-specific metabolic perturbations.

Results: Two machine learning models were constructed for the staged identification of abnormal early pregnancy. First, metabolic perturbations of TP were characterized by comparing TP with combined IUP (NP+SA) samples. In total, 77 differential metabolites and nine disturbed metabolic pathways were identified, which were mainly involved in arachidonic acid-related inflammation, TCA cycle dysfunction and tryptophan metabolic disorder. The LightGBM model based on LASSO-selected core metabolites showed valid performance in TP identification (AUC = 0.948, PR-AUC = 0.919, accuracy = 0.90). 15-deoxy-$\Delta^{12,14}$-prostaglandin J_2 and kynurenine were identified as key biomarkers for TP discrimination. Second, metabolic signatures distinguishing SA from NP were screened to evaluate embryonic developmental status. A total of 81 differential metabolites were obtained in SA samples, which were enriched in lipid peroxidation and ferroptosis-associated pathways. The LightGBM model for SA identification achieved valid predictive performance (AUC = 0.985, PR-AUC = 0.986, accuracy = 0.95). Glutathione and 3-hydroxyanthranilic acid were core biomarkers for SA prediction. Single-cell transcriptomic analysis further identified decidual cell states concordant with systemic serum metabolic alterations. TP decidua was characterized by a TP-enriched macrophage state with reprogrammed lipid inflammatory and energy metabolism profiles. SA decidua exhibited pro-inflammatory macrophage polarization, accompanied by downregulated *GPX4* expression and elevated ferroptosis-associated transcriptional signatures in endothelial cells and pro-inflammatory macrophages. These cell-type-specific transcriptional alterations

were concordant with, and may provide a cellular context for, the systemic metabolic perturbations observed in serum.

Conclusions: This study combines serum untargeted metabolomics and uterine decidual single-cell transcriptomics to characterize divergent metabolic dysregulations in TP and SA. The LightGBM metabolite-based models enable reliable early discrimination of ectopic pregnancy and impaired embryonic viability, offering potential auxiliary biomarkers for risk stratification in early pregnancy.

Keywords: Tubal pregnancy; Spontaneous abortion; serum metabolomics; machine learning; single-cell transcriptomics.

Graphical abstract

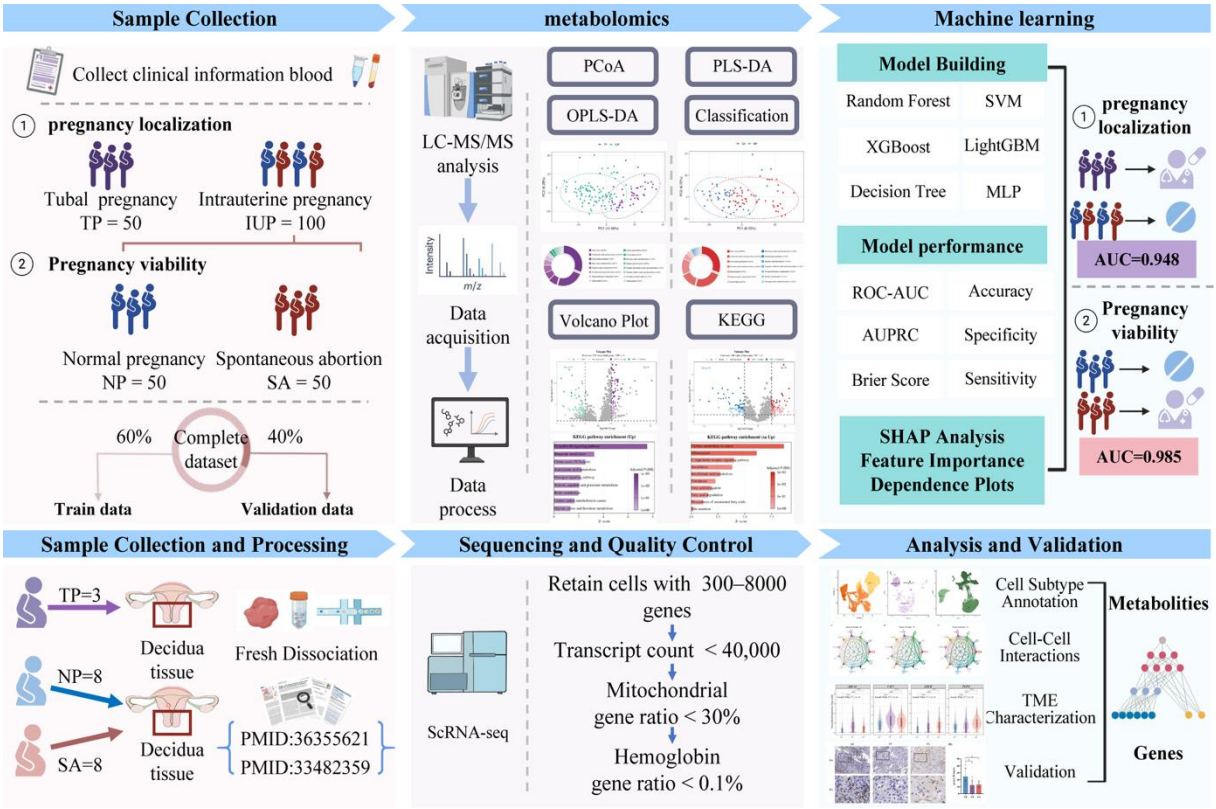


Figure 1. Graphical abstract

This multi-omics observational study enrolled three early-pregnancy cohorts including NP (n = 50), SA (n = 50), and unruptured TP (n = 50) for serum metabolomic profiling. Serum samples were split into a training set and a validation set at a 6:4 ratio to support machine-learning-driven diagnostic biomarker discovery. Decidual scRNA-seq data integrated herein comprised in-house generated sequencing data and two publicly available datasets. Integrative metabolomic and single-cell transcriptomic analyses identified candidate serum biomarkers and deciphered cellular-level pathological features underlying early-pregnancy complications.

Background

Tubal pregnancy (TP) and spontaneous abortion (SA) rank among the most prevalent and clinically high-burden complications in early pregnancy. They are associated with elevated acute maternal health risks, impaired long-term reproductive prognosis, and substantial physical and psychological distress in childbearing women (1, 2). TP is identified in roughly 1–2% of confirmed pregnancies and accounts for nearly 9% of early pregnancy-related maternal mortality globally, primarily due to unpredictable tubal rupture and subsequent hemorrhagic shock (1, 3). Meanwhile, SA affects up to 15% of clinically recognized pregnancies, frequently leading to persistent emotional distress, recurrent reproductive anxiety, and adverse subsequent pregnancy outcomes (2, 4). Although TP and SA differ fundamentally in pathological characteristics and gestational prognosis, their early clinical presentations are highly non-specific. Affected patients may present with overlapping symptoms including irregular vaginal bleeding and pelvic pain, or remain completely asymptomatic, which mimics the clinical manifestations of normal intrauterine pregnancy (NP) and substantially hinders early clinical differentiation (5-7).

Current clinical screening algorithms for suspected early pregnancy complications primarily rely on serial measurement of serum β-human chorionic gonadotropin (β-hCG) combined with transvaginal ultrasonography (TVUS) (8). Nevertheless, nearly 40% of initial TVUS examinations fail to identify definitive intrauterine or adnexal gestational structures, leading to the indeterminate diagnosis of pregnancy of unknown location (PUL) (9). Current clinical guidelines recommend repetitive β-hCG monitoring and sequential imaging follow-up within 48–72 h to distinguish TP, SA, and viable NP (6, 10). Such inherent diagnostic delays not only elevate the acute rupture risk of undiagnosed TP but also exacerbate prolonged psychological distress in patients with impending early pregnancy loss (11). In view of this unmet clinical bottleneck, there is an urgent demand for robust, minimally invasive serum biomarkers to enable accurate pregnancy localization and embryonic viability assessment at the early gestational stage, prior to the availability of definitive ultrasonic evidence.

Maternal serum metabolic signatures dynamically reflect core physiological events during early pregnancy, including uterine decidualization, trophoblast invasion, placental angiogenesis, and maternal-fetal immune homeostasis (12, 13). Pathological dysfunction of these gestational physiological processes triggers widespread metabolic perturbations in peripheral circulation, which emerge considerably earlier than imaging-detectable morphological lesions and serve as core pathogenic drivers underlying TP and SA progression (14). Untargeted metabolomics

enables high-throughput profiling of circulating small-molecule metabolites and has become a robust tool for discovering biomarkers across diverse adverse pregnancy conditions (15-17). Moreover, the integration of machine learning algorithms with high-dimensional metabolomic data can excavate subtle, disease-specific metabolic combinatorial signatures to precisely stratify heterogeneous pathological pregnancy subtypes, overcoming the insufficient diagnostic performance of single conventional indicators such as β-hCG and progesterone (12, 18, 19).

Despite these advances, existing metabolomic studies regarding TP and SA are largely confined to peripheral blood metabolic profiling at a single omic level (20, 21). Few investigations have integrated paired decidual tissue multi-omic data to trace the cellular and tissue origins of circulating metabolic dysregulation (22, 23). Against this research background, the present study integrated untargeted serum metabolomics, machine learning modeling, and decidual single-cell transcriptomics to construct a hierarchical diagnostic framework for early pathological pregnancy screening and further elucidate the disease-specific metabolic mechanisms of TP and SA. Two independent LightGBM diagnostic models were established based on LASSO-selected core metabolic signatures for stratified early pregnancy identification: one model was developed to distinguish unruptured TP from normal NP, and the other to differentiate non-viable SA from viable intrauterine pregnancy. All models were strictly trained and validated using grouped sample cohorts, with comprehensive diagnostic performance evaluated via AUC, sensitivity, specificity, and Brier score. Beyond diagnostic model construction, we systematically annotated differential metabolites and carried out KEGG enrichment analysis to map the principal metabolic pathways disrupted in each condition. Combined with decidual single-cell transcriptomic profiles, this study further uncovered distinct cell-specific metabolic reprogramming patterns underlying TP and SA, providing solid multi-omic evidence for their heterogeneous pathophysiological mechanisms. Collectively, this study aims to establish a rapid, minimally invasive auxiliary diagnostic strategy to optimize clinical early pregnancy triage, and offer novel mechanistic insights into early pregnancy complications for subsequent basic research and clinical translational exploration. The overall study design and analytical workflow are summarized in Figure 1.

Materials and Methods

Study population and design

Participant enrollment took place at the First Affiliated Hospital of Guangzhou University of Chinese Medicine, spanning the period from April 2025 to October 2025. A total of 150 eligible women with early pregnancy were recruited and divided into three groups (NP, SA, TP), with 50 participants in each group. Eligible participants were 18–40 years of age and had regular menstrual cycles; gestational age (6–8 weeks) was determined from the last menstrual period. Peripheral venous blood samples were collected from all subjects for untargeted serum metabolomics testing, and fresh decidual tissues were surgically obtained from patients in all three groups. Detailed inclusion criteria for each group are described below. The NP group consisted of healthy pregnant women who chose elective pregnancy termination for non-medical reasons; TVUS confirmed viable intrauterine pregnancy with visible embryonic cardiac activity. The TP group included patients diagnosed with hemodynamically stable unruptured tubal pregnancy, confirmed by serial serum β-hCG detection combined with TVUS manifestations of an empty uterine cavity and adnexal ectopic lesions. The SA group referred to patients diagnosed with early embryonic arrest, in whom the gestational sac size matched the estimated gestational age, yet no embryonic cardiac activity was detected on TVUS. Consistent exclusion criteria were adopted for all groups to rule out confounding variables: acute genital tract infection, congenital uterine malformations, uterine fibroids, adenomyosis, endocrine and metabolic disorders, severe cardiac, hepatic or renal insufficiency, autoimmune diseases, thrombotic diseases and coagulation dysfunction, chronic infectious diseases, chromosomal abnormalities of either parent, recent administration of hormone drugs or traditional Chinese medicine, long-term smoking and alcohol intake, and conception achieved through in vitro fertilization-embryo transfer (IVF-ET). Baseline demographic and obstetric information, alongside routine laboratory indices including serum β-hCG, progesterone, routine blood test and coagulation function, were collected via standardized questionnaire surveys and electronic medical record extraction.

Ethical approval for the research protocol was granted by the Ethics Committee of the First Affiliated Hospital of Guangzhou University of Chinese Medicine (Approval No. JY2025-057). Written informed consent was obtained from every participant prior to blood sampling and intraoperative decidual tissue collection.

Serum sample collection and pretreatment

Peripheral venous blood (5 mL) was drawn into vacuum tubes without anticoagulant. The tubes were left to stand at room temperature for 30 min to allow natural clotting and were then

centrifuged at 3000 rpm for 10 min at 4 °C. The upper serum layer was gently transferred into Eppendorf tubes and centrifuged a second time at 12,000 rpm for 10 min at 4 °C to pellet any residual cell debris. The resulting serum was stored at −80 °C until metabolomic analysis. For untargeted metabolomic profiling, a 500 μL serum aliquot was combined with 10 μL of internal standard solution (0.2 mg/mL L-2-chlorophenylalanine in methanol) and 1.5 mL of protein precipitation reagent (methanol:acetonitrile = 2:1, v/v). After thorough vortexing, the mixture underwent ultrasonic extraction at 5 °C for 30 min (40 kHz), was kept at −20 °C for 30 min to ensure adequate protein precipitation, and was then centrifuged at 13,000 rpm for 15 min at 4 °C. A 500 μL portion of the supernatant was transferred to a 1.5 mL centrifuge tube and evaporated to dryness under a gentle nitrogen stream. The residue was redissolved in 100 μL of 50% methanol, vortexed thoroughly, and sonicated on ice for 3 min. Following a final centrifugation (13,000 rpm, 10 min, 4 °C), 85 μL of the supernatant was transferred into an autosampler vial for LC-MS analysis. To monitor the stability of the analytical system throughout the detection process, quality control (QC) samples were generated by pooling 30 μL of supernatant from every study sample.

Decidual tissue collection and processing

Fresh decidual tissues were intraoperatively collected from patients in the NP, SA, and TP groups during elective curettage or laparoscopic surgery. Each tissue specimen was quickly washed with ice-cold sterile phosphate-buffered saline (PBS) to clear residual blood clots and mucus. Specifically, three fresh decidual samples obtained from TP patients were immediately processed into single-cell suspensions for in-house scRNA-seq experiments. The remaining decidual specimens from the three groups were fixed, embedded, and cryopreserved for later immunohistochemical and immunofluorescence staining.

UHPLC–MS analysis

Untargeted metabolomic profiling was carried out on an Ultimate 3000 UHPLC system interfaced with a Q Exactive Orbitrap mass spectrometer (Thermo Fisher Scientific, USA). Analytes were separated on a Hypersil GOLD column (100 × 2.1 mm, 1.9 μm) using 0.1% aqueous formic acid (mobile phase A) and acetonitrile (mobile phase B). The column was maintained at 40 °C, the flow rate was set to 0.3 mL/min, and the injection volume was 3 μL. The linear gradient program was: 0–10 min, 2%–50% B; 10–15 min, 50%–80% B; 15–20 min, 80%–98% B; 20–21 min, 98% B; and 21–23 min, 98%–2% B. The mass spectrometer was

equipped with a heated electrospray ionization (H-ESI) source and operated in both positive and negative ion modes. Full-scan spectra were collected at a resolution of 60,000 across an m/z range of 100–1500, and MS/MS fragmentation was performed at stepped normalized collision energies of 20, 40, and 60 eV. Optimized source parameters were as follows: spray voltage, 3.50 kV (positive mode) and 3.00 kV (negative mode); capillary temperature, 325 °C; sheath gas, 50 arb; auxiliary gas, 8 arb; and sweep gas, 1 arb. Data acquisition and instrument control were managed with Xcalibur 3.0 software.

Data processing and metabolite identification

Before statistical analysis, the raw LC-MS data were filtered under unified criteria: metabolic features detected in more than 80% of samples were retained, missing values were imputed with half of the minimum valid value of the dataset, and unstable features showing a relative standard deviation (RSD) $\geqslant$ 30% among QC samples were excluded. The stability and reproducibility of the entire detection system were evaluated by overlaying total ion chromatograms (TICs) of all QC samples and conducting Pearson correlation and hierarchical clustering analysis, while metabolite identification was accomplished using Compound Discoverer 3.0 software via spectral matching against mzCloud and HMDB databases with a mass error threshold of 5 ppm, and all annotated metabolites conformed to the Metabolomics Standards Initiative (MSI) Level 2 and Level 3 criteria based on systematic MS/MS spectral verification.

Metabolomic Analysis

Before multivariate analysis, metabolite data were normalized to the total peak area, log10-transformed, and auto-scaled. All statistical analyses were conducted in R software. An unsupervised principal coordinate analysis (PCoA) based on metabolic profile similarity was applied to evaluate the overall data distribution and detect outliers. Two supervised OPLS-DA and PLS-DA models were constructed for subgroup comparison, including pregnancy location (IUP vs. TP) and pregnancy viability (SA vs. NP) grouping strategies. Model reliability was verified via 1000-permutation tests. Differential metabolites were identified by integrating the variable importance in projection (VIP) values from OPLS-DA with limma-based univariate analysis. Metabolites meeting VIP > 1.5, adjusted $P < 0.05$, and $|\log_2 FC| > 0.25$ were regarded as differential metabolites and visualized with volcano plots and clustering heatmaps.

Statistical analysis and model building

Through stratified sampling, all enrolled samples were randomly assigned to a training set and a validation set at a 6:4 ratio. To prevent data leakage, feature selection and model training were restricted to the training set, whereas the validation set was reserved exclusively for final model evaluation. Differential metabolites were preliminarily screened in the training set with the thresholds of adjusted $P < 0.05$ and $|\log_2 FC| > 0.5$, followed by OPLS-DA screening with VIP > 1.5. The overlapping metabolites were further optimized by LASSO regression with 5-fold cross-validation (3 repeats) and the final biomarker panel was determined according to the lambda.1se criterion. Predictive models for pregnancy location and viability discrimination were constructed with six machine learning algorithms: decision tree (DT), random forest (RF), extreme gradient boosting (XGBoost), light gradient boosting machine (LightGBM), multi-layer perceptron (MLP), and radial-basis support vector machine (RSVM). Grid search was used to optimize hyperparameters, and model performance was primarily evaluated by the area under the receiver operating characteristic curve (AUC) obtained from 5-fold cross-validation. To assess model generalization in the validation set, multiple metrics were adopted, including AUC, the area under the precision-recall curve (AUPRC), accuracy, sensitivity, specificity, and Brier score. The six evaluation metrics of each model were summarized and visualized as multidimensional radar charts for intuitive comparison. The overall machine-learning analytical pipeline is illustrated in Figure S1.

Model interpretation

To clarify the contribution of individual features, Shapley Additive exPlanations (SHAP) values were computed with the fastshap package in R (version 4.2.1). This approach quantified each metabolite's impact on the model's predictive output, providing both global importance and local interpretability.

Single-cell RNA Sequencing and Data Processing

Fresh decidual tissues obtained from three patients with TP were processed into single-cell suspensions through tissue dissection and collagenase digestion. Single-cell libraries were constructed and subjected to high-throughput sequencing on the 10x Genomics platform. The raw sequencing data were processed with Cell Ranger (v3.0.0) and mapped to the human GRCh38 reference genome. The Cellranger count pipeline was applied for data preprocessing,

including barcode and UMI reading, RNA read trimming, STAR-based genome alignment, gene read annotation, UMI correction, valid cell barcode screening, and final generation of single-cell gene expression matrices. Publicly available gestational age-matched (6–8 weeks) decidual single-cell RNA-seq datasets of early miscarriage were integrated to supplement our in-house sequencing data (PMID: 36355621 (24), 33482359 (25)). Notably, recurrent miscarriage is clinically defined as two or more spontaneous pregnancy losses (26); the decidual samples in both public datasets were collected at such events, with fetal or parental chromosomal abnormalities excluded and gestational ages matched to our cohorts. All downstream analyses were conducted with the Seurat package (v4.3.0) in R. During preliminary quality control, genes expressed in fewer than three cells, together with cells harboring < 200 detected genes, were removed. Strict filtering thresholds were further applied to retain high-quality cells: nFeature RNA ranging from 300 to 8000, mitochondrial gene proportion < 30%, and hemoglobin gene proportion < 10%. The top 2000 highly variable genes were used for principal component analysis (PCA), and cross-batch effects were corrected with the Harmony algorithm.

Cell Clustering, Annotation and Differential Expression Analysis

The FindVariableFeatures function was applied to screen highly variable genes, and the expression matrix was normalized with ScaleData. PCA was performed on variable genes, and the optimal 22 principal components were determined according to ElbowPlot results for subsequent dimensionality reduction. Unsupervised clustering of cells was performed with the FindNeighbors and FindClusters functions at an optimized resolution, and the resulting cell clusters were visualized by UMAP embedding. Representative canonical marker genes were applied to define and annotate each cell subtype. Differential expression between cell clusters was assessed with the Wilcoxon rank-sum test implemented in the Seurat package, and the Benjamini–Hochberg procedure was applied for false discovery rate correction. Genes showing $|\log_2 FC| > 0.25$ with adjusted $P < 0.05$ were defined as significant differentially expressed genes (DEGs). Volcano plots of DEGs were visualized using the ggplot 2 package.

Functional Enrichment and Pathway Scoring Analysis

Enrichment analysis of Gene Ontology (GO) biological processes was conducted with the clusterProfiler package in R. DEG lists were converted from Gene symbols to Entrez IDs, and the enrichGO function was used to enrich functional biological processes to clarify the potential

biological roles of screened DEGs. To quantify metabolic pathway activity at the single-cell level, lipid metabolism-related gene sets, including glycerophospholipid metabolism and fatty acid metabolism, were curated from the KEGG database. Single-cell pathway module scores were computed using the AddModuleScore function in the Seurat package with default parameters, and the resulting scores were compared across macrophage subsets and among the NP, SA and TP cohorts. Using the same scoring framework, a single-cell ferroptosis susceptibility index and pro-inflammatory/M1-like transcriptional scores were derived from curated ferroptosis-associated gene sets (27) and canonical M1 macrophage marker gene sets (28) respectively.

Cell–Cell Communication Analysis

Cell–cell communication analysis was conducted using CellChat (v1.6.1) based on the human CellChatDB human database. CellChat objects were constructed separately for TP, NP, and SA groups using normalized expression data and cell annotations. Low-confidence interactions supported by fewer than 10 cells were filtered, and signal intensities were corrected with human PPI networks.

Oil Red O staining

Lipid accumulation within decidual specimens was assessed via Oil Red O histological staining. Freshly prepared frozen tissue slices were rapidly washed with 60% isopropanol to remove residual water impurities, then incubated in configured Oil Red O staining solution for 12 minutes at room temperature. Subsequent hematoxylin counterstaining was performed to label cell nuclei. After gradient dehydration and transparent treatment, all sections were mounted and sealed for preservation. Whole-slide pathological imaging was performed using the Pannoramic MIDI digital scanning platform to visualize lipid deposition characteristics across distinct experimental groups. The mean optical density of positively stained lipid areas was quantitatively analyzed using ImageJ software for further statistical comparison.

Immunofluorescence Staining

Immunofluorescence assay was applied to detect the endothelial biomarker CD31 expression in decidual tissues. Paraffin-embedded decidual samples were continuously sliced into 4 μm sections and completely deparaffinized with xylene gradient solution. Microwave-based antigen retrieval was sustained for 12 minutes to fully expose tissue antigen epitopes.

Tissue sections were incubated overnight at 4 °C with diluted CD31 monoclonal antibody (PECAM, MA-3100; 1:1000 working concentration). After three rounds of PBS rinsing (3 minutes per wash), tissue slides were incubated with matched Alexa Fluor-conjugated secondary antibody for 60 minutes at 37 °C. Following additional PBS cleaning, cell nuclei were stained with DAPI solution (200 ng/mL) for 3 minutes under ambient temperature conditions before microscopic observation.

Statistical analysis

Single-cell transcriptomic data analysis and graphical visualization were performed in R software (v4.1.3) with the Seurat and ggplot2 packages. All immunohistochemical experiments were performed in no less than three independent replicates. Two-group comparisons were performed with unpaired two-tailed Student's t-tests, and multi-group comparisons with one-way ANOVA. GraphPad Prism 10 software was adopted for statistical analysis and result visualization. Pearson correlation coefficient was used for correlation analysis. The thresholds for statistical significance were set as follows: *$P < 0.05$, ** $P < 0.01$, *** $P < 0.001$, **** $P < 0.0001$; ns denoted no significant difference ($P \geqslant 0.05$).

Results

Baseline demographic and clinical characteristics of participants

In total, 150 women with confirmed first-trimester early-pregnancy status were enrolled and stratified into three study cohorts: normal intrauterine pregnancy (NP, n = 50), spontaneous abortion (SA, n = 50), and unruptured tubal pregnancy (TP, n = 50). The participant screening flowchart and cohort assignment strategy are illustrated in Figure 2. Baseline demographic features, obstetric background information, serum β-hCG and progesterone measurements are summarized in Supplementary Table S1, whereas admission-derived routine hematology and coagulation profiles are provided in Supplementary Table S2. No statistically significant inter-group differences were detected in maternal age ($P = 0.306$), pre-pregnancy BMI, gravidity, parity, history of prior abortion, or other obstetric and lifestyle-related covariates (all $P > 0.05$). Only subjects with regular menstrual cycles were recruited, and all patients fell within a unified clinical sampling window of 6–8 weeks of amenorrhea.

Serum β-hCG median values were markedly lower in the TP group (2300.50 IU/L, IQR 1105.75–4479.50) than in NP (4849.50 IU/L, IQR 3350.75–8324.50) and SA (4901.50 IU/L, IQR 2618.50–6611.00). The Kruskal-Wallis H test with Dunn's post-hoc comparisons confirmed that β-hCG was lower in TP than in NP and SA (both $P < 0.001$), whereas β-hCG was comparable between NP and SA ($P > 0.05$). Serum progesterone showed a similar pattern. One-way ANOVA revealed an overall inter-group difference ($P = 0.013$). Post-hoc pairwise comparisons demonstrated reduced progesterone in TP (14.27 ± 6.47 ng/mL) compared with NP (18.40 ± 7.70 ng/mL, $P < 0.05$) and SA (16.17 ± 6.49 ng/mL, $P < 0.05$), whereas SA and NP did not differ significantly ($P > 0.05$). Of note, although β-hCG and progesterone showed statistically significant inter-group differences, individual values exhibited substantial overlap across cohorts. Reliable individual-patient discrimination cannot be achieved using β-hCG or progesterone alone, highlighting the clinical demand for additional objective auxiliary diagnostic markers.

Complete blood count and coagulation test results for all participants are compiled in Supplementary Table S2. Several hematological parameters exhibited significant inter-group discrepancies. Platelet distribution width (PDW), an established surrogate marker for platelet activation, was significantly elevated in the SA group compared with the NP and TP groups (overall $P = 0.007$), indicating enhanced platelet activation and systemic inflammatory responses associated with early pregnancy loss (29, 30). The TP group presented decreased peripheral blood cell counts, with significantly lower absolute neutrophil counts than the SA group ($P = 0.027$) and reduced red blood cell counts relative to NP controls ($P = 0.049$). These hematological alterations are consistent with previously reported blood cell perturbations characteristic of tubal implantation (31). No significant inter-group differences were observed in core coagulation indices, including prothrombin time (PT) and activated partial thromboplastin time (APTT).

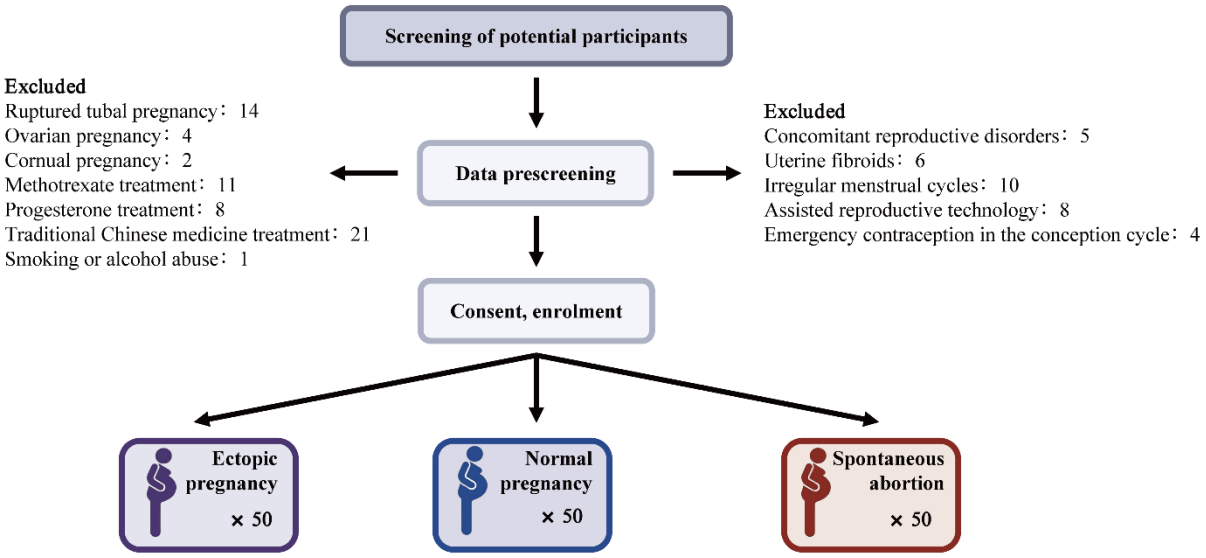


Figure 2. Flowchart illustrating participant screening, exclusion criteria and final cohort allocation of the present study.

Metabolic Profiling Distinguishes Combined IUP from TP.

We first conducted QC and global separation analysis for untargeted metabolomic data. The QC total ion chromatograms exhibited stable chromatographic peaks in both the positive and negative ion modes (Figure S2A, S2C). Strong pairwise correlations ($r > 0.80$) and tight clustering of QC replicates confirmed stable instrumental performance and high-quality metabolomic data (Figure S2B, S2D). Unsupervised PCoA revealed clear metabolic distinction between IUP and TP groups, with significant intergroup dissimilarity validated by PERMANOVA ($R^2 = 0.094$, $P = 0.001$; Figure 3A). The supervised OPLS-DA model achieved complete group separation (Figure 3B), with satisfactory fitting (cumulative $R^2Y = 0.937$) and predictive capacity (cumulative $Q^2 = 0.802$). PLS-DA reproduced consistent separation (Figure S3A), and one thousand permutation tests excluded model overfitting (Figure S3B, S3C)

Differential metabolites were screened under consistent criteria (VIP > 1.5, $|\log_2 FC| > 0.25$, and adjusted $P < 0.05$). Overall, 77 metabolites exhibited significant abundance alterations in TP relative to IUP, of which 54 were up-regulated and 23 were down-regulated (Figure 3C, Supplementary Table S3). KEGG enrichment analysis was conducted for the metabolites up-regulated in TP to identify perturbed biological pathways (Figure 3D, Supplementary Table S4). The top-ranked enriched pathway with the highest Z-score and nominal statistical significance was the Fcε RI signalling pathway. Other top-listed pathways included butanoate metabolism, the TCA cycle, arachidonic acid metabolism, and glucagon signalling pathway. Notable enrichment of the TCA cycle points toward disturbed mitochondrial-related metabolism among

TP patients, which is consistent with prior mechanistic observations of ectopic trophoblast injury (32). We further selected the top-30 metabolites ranked by VIP value and combined these molecules with clinically relevant differential indicators, including serum β-hCG, progesterone, neutrophil count and red-blood-cell count, for bidirectional hierarchical clustering analysis (Figure 3E). These metabolites mainly fell into amino-acid, fatty-acid, lipid and organic-acid classes, and samples showed distinct clustering patterns consistent with pregnancy phenotypes. Several high-VIP metabolites presented phenotype-specific abundance profiles: estrone sulfate and prostaglandin F2α were markedly decreased in TP samples, whereas sphingosine-1-phosphate was substantially accumulated. These metabolites are involved in steroid biosynthesis and sphingolipid-driven inflammatory signalling, suggesting disrupted steroid metabolism and inflammatory responses during tubal gestation (33).

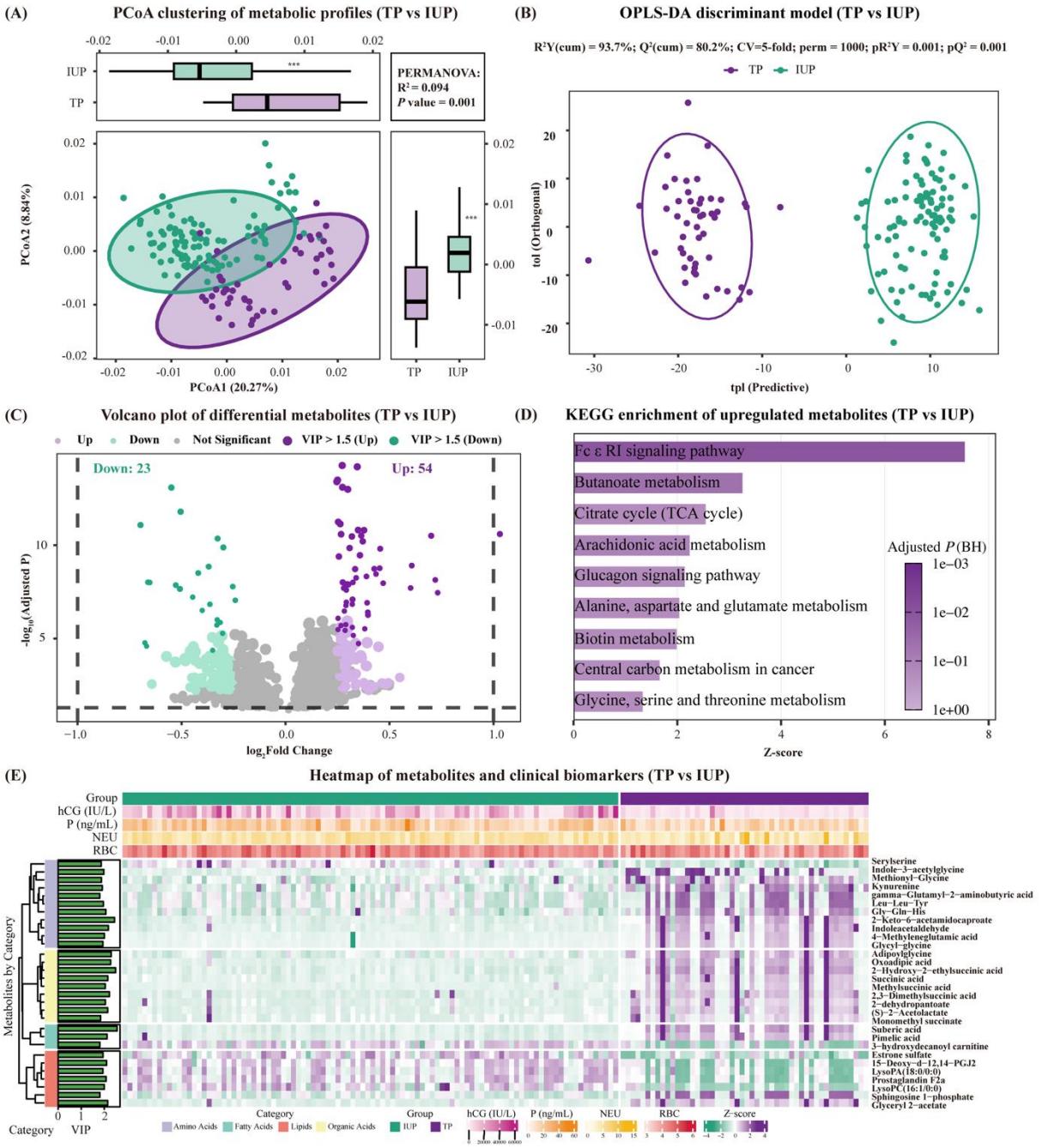


Figure 3. Circulating metabolic differences between the combined IUP and TP cohorts.

(A) Unsupervised PCoA based on global serum metabolome profiles. Each dot represents one participant; ellipses denote 95% confidence intervals for each group. PERMANOVA was performed to evaluate inter-group metabolic dissimilarity.
(B) Supervised OPLS-DA score plot demonstrating metabolic separation between IUP and TP cohorts.
(C) Volcano plot of differentially abundant metabolites. Purple dots: metabolites upregulated in TP; green dots: metabolites downregulated in TP relative to IUP.
(D) Bar plot showing top-ranked KEGG enrichment pathways for TP-elevated metabolites. Bar height corresponds to enrichment Z-score, and bar colour encodes BH-adjusted P-values; darker colour indicates higher statistical significance.
(E) Bidirectional hierarchical-clustering heatmap integrating top-30 VIP-ranked metabolites and key clinical biomarkers (β-hCG, progesterone, NEU, RBC). Metabolite annotations are

displayed on the right-side vertical axis. The left sidebar presents VIP values and metabolite chemical categories. Top-row sample annotations distinguish IUP (green) and TP (purple).

Metabolic Profiling Distinguishes NP from Early SA.

Distinguishing benign early pregnancy outcomes is critical for optimizing clinical management after excluding ectopic gestation. This study further profiled serum metabolomic differences between NP and SA to identify metabolic signatures indicative of early pregnancy loss. Unsupervised PCoA revealed global metabolic divergence between the two groups (Figure 4A). PERMANOVA corroborated statistically significant inter-group metabolic dissimilarity (R^2 = 0.088, P = 0.001), in agreement with pairwise metabolic-profile distance distributions. The supervised OPLS-DA model yielded sample-level metabolic separation between NP and SA (Figure 4B), with favourable model fitness (cumulative R^2Y = 0.970) and predictive capacity (cumulative Q^2 = 0.828). One-thousand-iteration permutation testing excluded model overfitting (Figure S4B, S4C; p(R^2Y) = 0.001, p(Q^2) = 0.001). PLS-DA further reproduced consistent inter-group metabolic clustering patterns (Figure S4A). Using unified filtering criteria (VIP > 1.5, $|\log_2 FC| > 0.25$, BH-adjusted $P < 0.05$), 81 metabolites were found to show significant abundance changes in SA relative to NP, comprising 38 up-regulated and 43 down-regulated molecules (Figure 4C, Supplementary Table S5).

KEGG enrichment analysis was conducted for the metabolites up-regulated in SA. The top-ranked pathways included choline metabolism in cancer and efferocytosis with nominal statistical significance, along with the C-type lectin receptor signaling pathway, amoebiasis, and arachidonic acid metabolism (Figure 4D, Supplementary Table S6). The ferroptosis pathway was prominently enriched among the ranked pathways, implying that sustained oxidative lipid injury may participate in SA pathogenesis (34). Multiple fatty acid-related pathways, namely fatty acid elongation, fatty acid degradation, and unsaturated fatty acid biosynthesis, were markedly perturbed, offering metabolic evidence supporting excessive lipid peroxidation and subsequent ferroptosis activation in SA.

We integrated the top-30 VIP-ranked metabolites with differential clinical indicators (serum β-hCG, progesterone and PDW) for bidirectional hierarchical-clustering analysis (Figure 4E). Representative high-VIP metabolites displayed phenotype-specific abundance profiles. SA samples exhibited higher levels of lipid- and sphingolipid-related pathogenic metabolites, including 9,10-epoxystearic acid, phytosphingosine and SM(d18:1/22:1), accompanied by decreased levels of 4-Hydroxyestrone-2-S-glutathione, tetrahydrofolic acid and O-palmitoylcarnitine. These molecular patterns further supported lipid remodelling,

disturbed antioxidant defence and ferroptosis-related metabolic features in SA. Clinical biomarkers exhibited coordinated shifts alongside metabolomic signatures between groups. SA patients had lower circulating β-hCG and progesterone concentrations, whereas PDW was increased. PDW serves as a surrogate marker for platelet activation; activated platelets can secrete lipid-derived mediators that modulate oxidative metabolism (35).

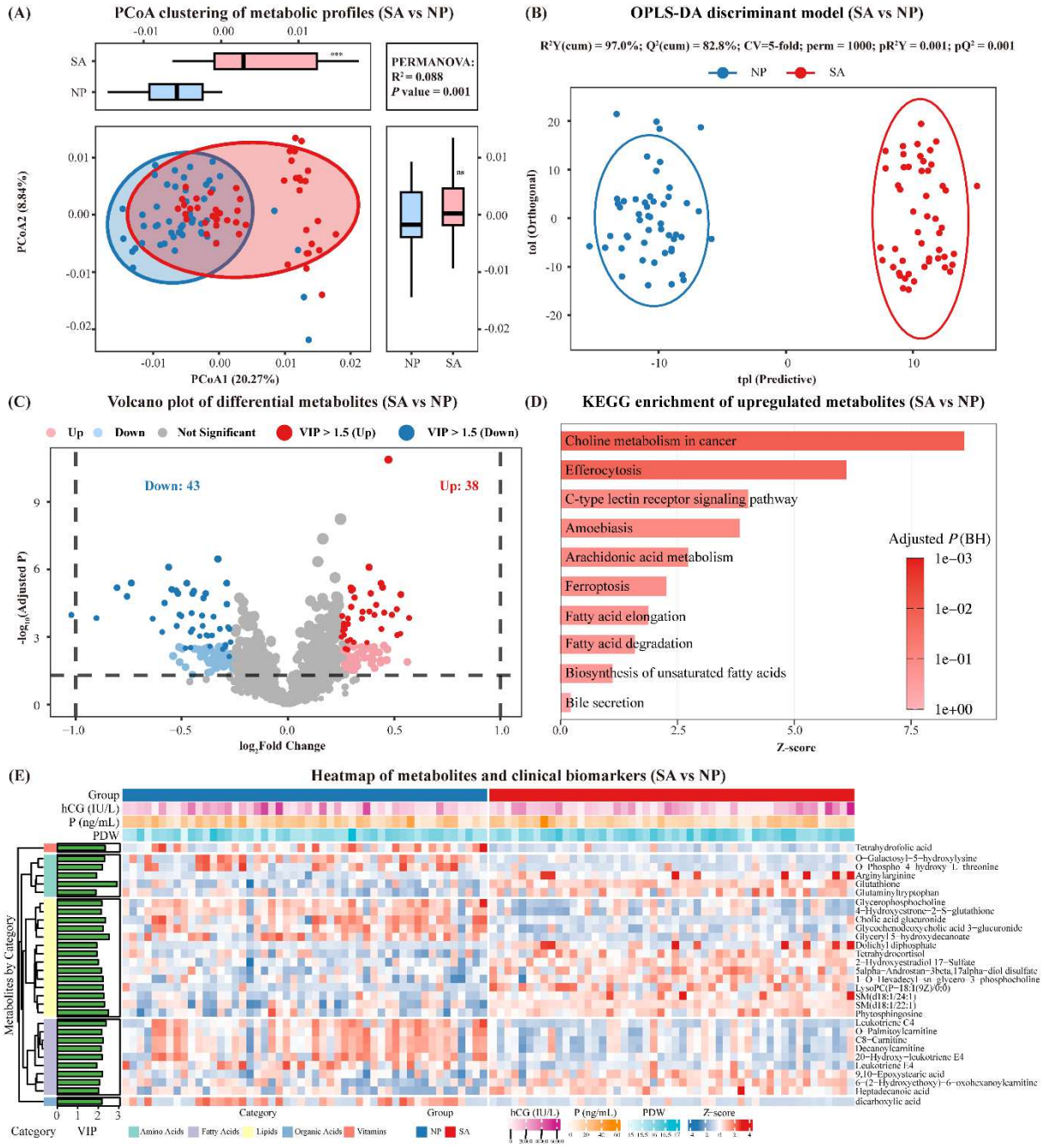


Figure 4. Circulating metabolic differences between NP and SA.

(A) Unsupervised PCoA based on global serum metabolome profiles. Each dot represents an individual participant; ellipses denote 95% confidence intervals for each group. PERMANOVA was performed to evaluate inter-group metabolic dissimilarity.

(B) Supervised OPLS-DA score plot showing the metabolic separation of the NP and SA cohorts.
(C)Volcano plot of differentially abundant metabolites; red dots denote metabolites upregulated in SA, and blue dots denote those downregulated in SA relative to NP.
(D) Bar plot showing top-ranked KEGG enrichment pathways for SA-elevated metabolites. Bar height corresponds to enrichment Z-score, and bar colour encodes BH-adjusted P-values; darker colour indicates higher statistical significance.
(E) Bidirectional hierarchical-clustering heatmap integrating the top 30 VIP-ranked metabolites and key clinical biomarkers (β-hCG, progesterone, PDW). Metabolite annotations are displayed on the right vertical axis. The left sidebar presents VIP values and metabolite chemical categories. Top-row sample annotations distinguish NP (blue) and SA (red) samples.

Identification of core metabolite panels for the two-stage early pregnancy outcome prediction model

Our biomarker evaluation strategy follows the sequential clinical assessment of early pregnancy complications (Figure 5A). In clinical practice, early gestation with undetermined location presents diagnostic difficulty, as tubal pregnancy, spontaneous abortion and normal intrauterine pregnancy may exhibit overlapping early clinical characteristics. Delayed recognition of tubal pregnancy confers risks of tubal rupture and hemorrhage, rendering its exclusion the primary clinical priority. Subsequent risk stratification for spontaneous abortion is then conducted among confirmed intrauterine pregnancies (8, 36). Accordingly, we first identified a metabolite signature discriminating TP from IUP, and then constructed a signature for SA risk stratification among confirmed IUP cases.

For TP versus IUP discrimination, we identified 26 significantly altered metabolites in the training cohort, including 11 upregulated and 15 downregulated metabolites in TP relative to combined IUP (Figure S5A). The three-repeat 5-fold cross-validation curve for LASSO hyperparameter tuning is shown in Figure S5B, and the coefficient-path plot showing feature coefficient shrinkage with rising penalty intensity is presented in Figure S5C. Eight metabolites with non-zero coefficients constituted the TP diagnostic signature (Figure S5D, Supplementary Table S7): kynurenine, glycerol 3-phosphate, glycodeoxycholic acid, LysoPS(16:0/0:0), decanoylcarnitine, prostaglandin J_2, estrone sulfate and 15-deoxy-$\Delta^{12,14}$-prostaglandin J_2. Coefficient analysis showed that kynurenine and glycerol 3-phosphate were positively associated with TP risk, whereas 15-deoxy-$\Delta^{12,14}$-prostaglandin J_2, estrone sulfate, prostaglandin J_2, decanoylcarnitine, LysoPS(16:0/0:0) and glycodeoxycholic acid showed negative coefficients, corresponding to higher abundance in IUP. We constructed six machine-learning classification models based on this 8-metabolite panel and validated them in the internal validation set (Figure 5B), with full performance metrics listed in Supplementary

Table S8. In internal validation, the LightGBM model achieved the best diagnostic performance (ROC-AUC = 0.948, PR-AUC = 0.919; accuracy, sensitivity and specificity = 0.90; Brier-score = 0.105), indicating good discrimination and probability calibration. Random Forest exhibited suboptimal performance (ROC-AUC = 0.895), and Decision Tree performed poorest (ROC-AUC = 0.800, PR-AUC = 0.686). SHAP analysis quantified metabolite predictive contributions in the LightGBM model (Figure 5C). The top four contributors were 15-deoxy-$\Delta^{12,14}$-prostaglandin J_2, kynurenine, glycerol 3-phosphate, and LysoPS(16:0/0:0). SHAP dependence plots revealed that higher abundances of kynurenine and glycerol 3-phosphate were associated with elevated TP risk, whereas higher levels of 15-deoxy-$\Delta^{12,14}$-prostaglandin J_2, LysoPS(16:0/0:0), estrone sulfate and glycodeoxycholic acid corresponded to intrauterine pregnancy. These metabolites participate in multiple regulatory pathways governing early-pregnancy physiology (37-40). Kynurenine shapes maternal–fetal immune tolerance through tryptophan catabolism. Prostaglandin derivatives modulate extravillous trophoblast invasion and uterine microenvironment remodelling. Glycerophospholipids and medium-chain acylcarnitines influence trophoblast membrane fluidity and embryonic mitochondrial energy metabolism. Steroid and bile acid metabolites maintain endocrine homeostasis during normal intrauterine pregnancy.

For SA versus NP discrimination, 34 differential metabolites were screened in the training set: 10 upregulated and 24 downregulated metabolites in SA relative to NP (Figure S6A). The three-repeat 5-fold cross-validation curve for LASSO hyperparameter tuning is shown in Figure S6B, and the LASSO coefficient-path plot of coefficient shrinkage along increasing penalty strength is presented in Figure S6C. Eight metabolites retaining non-zero regression coefficients formed the SA diagnostic signature (Figure S6D, Supplementary Table S9): glutathione, leukotriene E4, 3-hydroxyanthranilic acid, hexenoylcarnitine, 20-hydroxy-leukotriene E4, cholic acid glucuronide, glycochenodeoxycholic acid 3-glucuronide, and leukotriene C4. Coefficient results showed glutathione, leukotriene E4, 3-hydroxyanthranilic acid and hexenoylcarnitine had positive coefficients correlated with higher SA risk; leukotriene C4, cholic acid glucuronide, glycochenodeoxycholic acid 3-glucuronide and 20-hydroxy-leukotriene E4 had negative coefficients linked to uncomplicated intrauterine pregnancy. We trained six supervised machine-learning classifiers using this 8-metabolite signature and assessed performance in the internal validation set (Figure 5D; Supplementary Table S10). Consistent with the TP model, LightGBM yielded optimal SA risk-stratification performance (ROC-AUC = 0.985, PR-AUC = 0.986; accuracy, sensitivity

and specificity = 0.95; Brier-score = 0.084), showing strong discriminative power and reliable probability calibration. Random Forest and XGBoost achieved comparable performance (ROC-AUC = 0.970 each), while Decision Tree had the lowest predictive efficacy (ROC-AUC = 0.825, PR-AUC = 0.800). SHAP analysis quantified the contribution and directional effects of SA-related biomarkers in the LightGBM model (Figure 5E). Ranked by mean absolute SHAP values, the top four metabolites were 3-hydroxyanthranilic acid, glutathione, leukotriene E4, and cholic acid glucuronide. Higher 3-hydroxyanthranilic acid and glutathione levels correlated with elevated SA risk, whereas increased leukotriene E4 and cholic acid glucuronide abundance reflected uncomplicated intrauterine pregnancy.

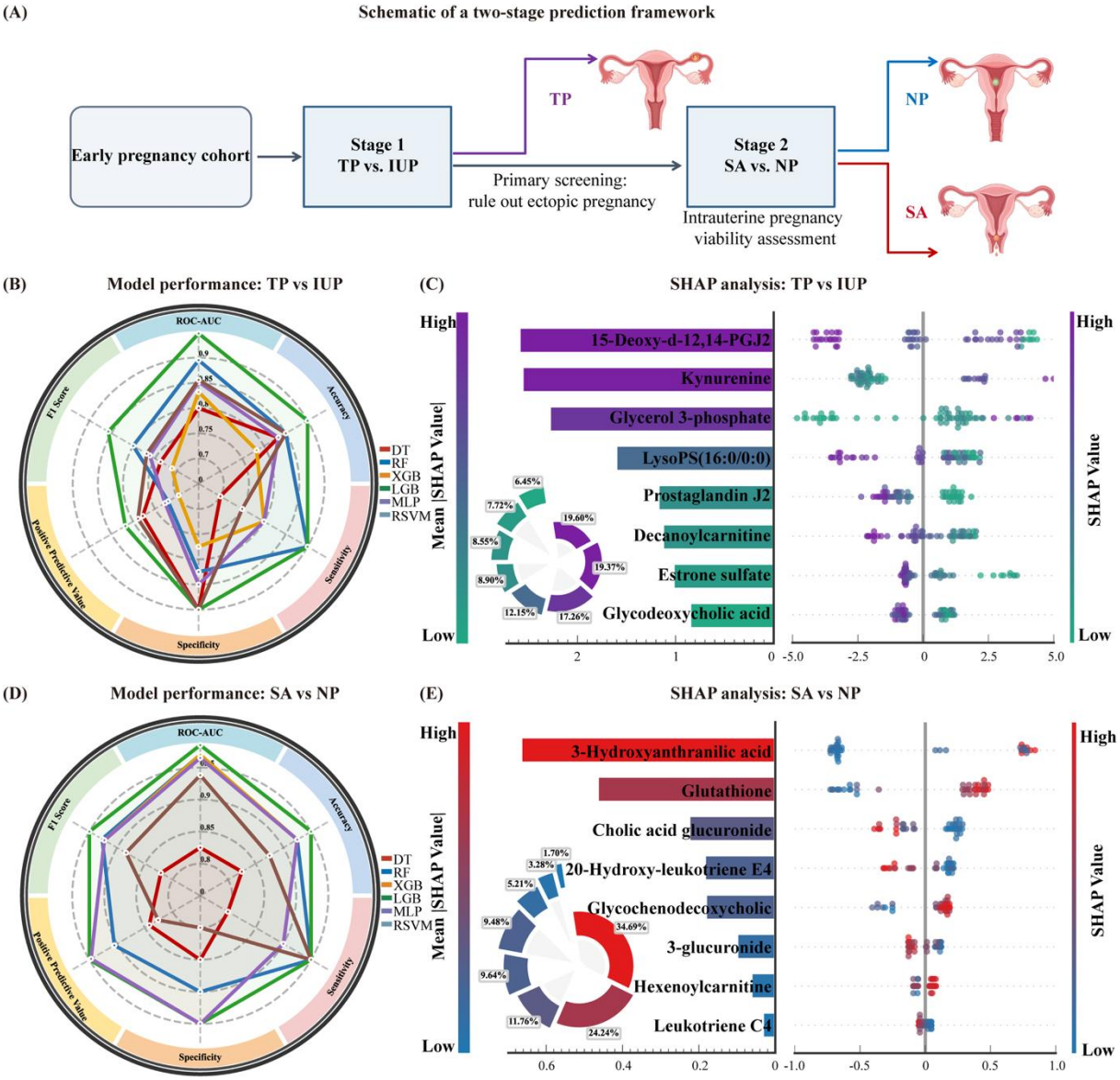


Figure 5. Metabolite signatures allow hierarchical discrimination of early pregnancy outcomes.

(A) Schematic diagram illustrating the two-stage hierarchical prediction framework for early pregnancy risk stratification. Stage 1 distinguishes TP from IUP; samples classified as IUP proceed to Stage 2 to discriminate NP from SA.
(B) Multidimensional radar chart summarizing six evaluation metrics for machine learning models discriminating TP from IUP.
(C) SHAP interpretability analysis of the optimal LightGBM model for TP/IUP classification. Left bar plot: metabolite ranking by mean absolute SHAP value; right scatter plot: directional predictive effects of core biomarkers.
(D) Multidimensional radar chart summarizing six evaluation metrics for machine learning models discriminating SA from NP.
(E) SHAP interpretability analysis of the optimal LightGBM model for SA/NP classification. Left bar plot: metabolite ranking by mean absolute SHAP value; right scatter plot: directional predictive effects of core biomarkers.

Integrated Metabolic Network Identifies Lipid and Arachidonic Acid Dysregulation and Linked Mitochondrial Dysfunction in Tubal Pregnancy

To systematically dissect biological mechanisms underlying metabolic dysregulation in TP, we mapped key differential metabolites onto canonical KEGG cascades (Figure 6). Consistent with preceding enrichment results, widespread disturbance of lipid metabolism, especially arachidonic acid signaling, was associated with inflammatory lipid signaling and alterations in mitochondrial-related metabolism. The integrated pathway diagram outlines interlinked metabolic disturbances participating in TP pathogenesis, with quantitative metabolite alterations validated by normalized serum abundance comparison between groups.

Glycerophospholipid-associated inflammatory signaling is activated in serum samples from TP patients. Elevated LysoPC(10:0/0:0) and arachidonic acid initiate downstream pro-inflammatory cascades. As a vital upstream lipid inflammatory precursor, arachidonic acid drives production of prostaglandin D2 (PGD2) and multiple leukotriene mediators via cyclooxygenase and lipoxygenase pathways. These alterations may be compatible with an inflammatory milieu associated with tubal pregnancy (41).

Furthermore, pathological reprogramming of tryptophan catabolism occurs in TP, with markedly upregulated kynurenine and indoleacetaldehyde. Excessive kynurenine disturbs maternal-fetal immune tolerance and amplifies systemic inflammatory signaling, further compromising the tubal microenvironment required for embryonic survival (42). Collectively, glycerophospholipid and arachidonic acid metabolic disturbance represents the primary metabolic abnormality in tubal pregnancy. These circulating metabolic signatures reflect local pathological changes, collectively contributing to the formation of an oxidative, inflammatory, energy-deficient tubal microenvironment that restricts embryonic development (32).

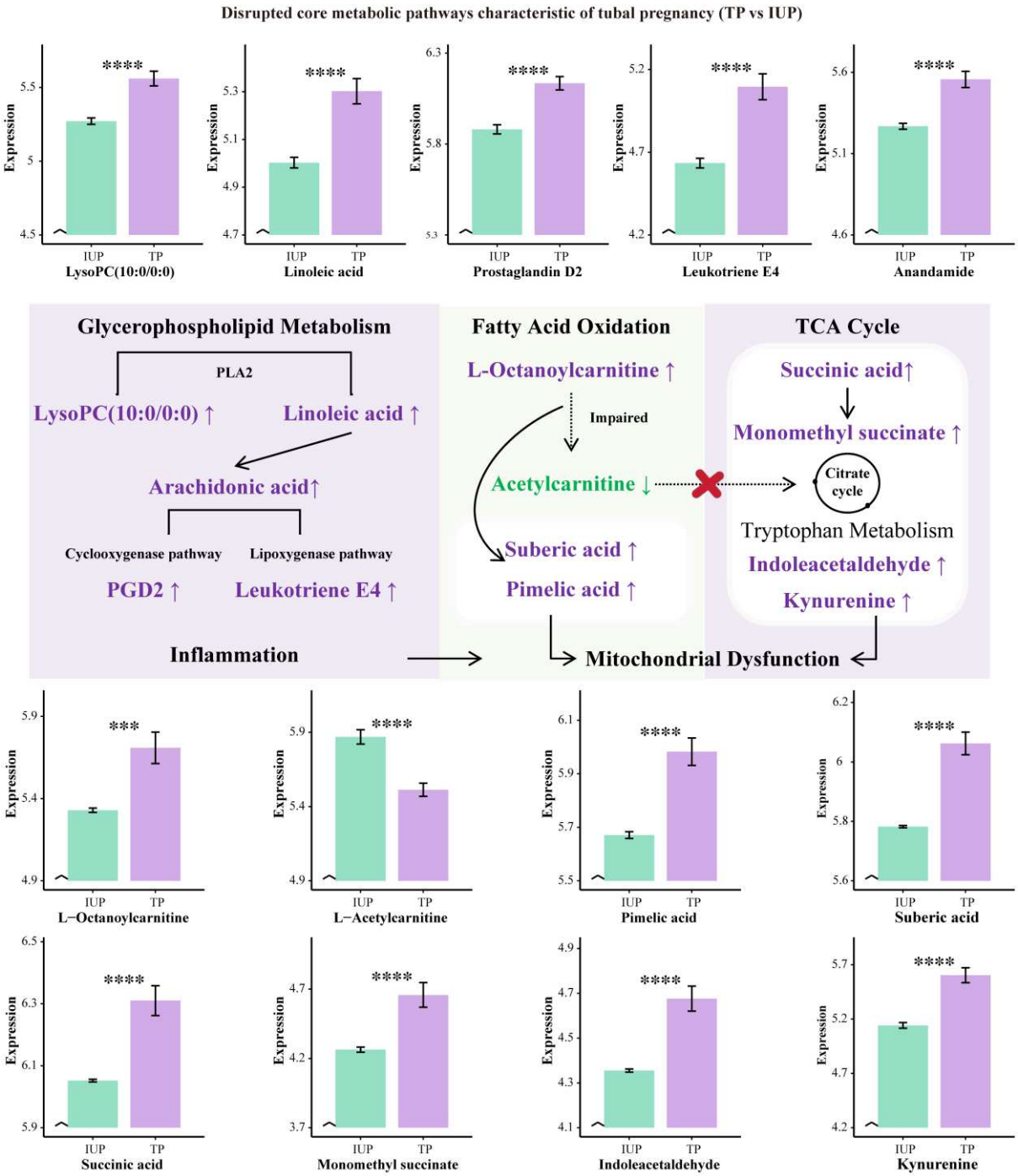


Figure 6. Integrated schematic of core dysregulated metabolic pathways distinguishing TP from IUP.

The central network illustrates crosstalk among lipid-inflammatory cascades, impaired mitochondrial fatty-acid oxidation, disrupted TCA-cycle flux, and tryptophan-dependent immune metabolism. Upward arrows denote metabolites significantly elevated in TP; downward arrows indicate metabolites depleted in TP. Surrounding bar charts present normalized relative serum expression of key nodal metabolites. Values are shown as the mean ± standard error of the mean (SEM). Statistical significance: ***$P < 0.001$, **** $P < 0.0001$.

Integrated Metabolic Pathway Network Identifies Lipid Peroxidation-Driven Ferroptosis and Systemic Oxidative Stress as Core Pathogenic Hallmarks of Early Spontaneous Abortion

To dissect metabolic dysregulation and potential pathogenic mechanisms underlying SA, we mapped key SA-specific differential metabolites onto canonical KEGG signaling cascades, and constructed a ferroptosis-centered metabolic regulatory network (Figure 7). Metabolic disturbances in SA represent a metabolic pattern compatible with enhanced lipid peroxidation and ferroptosis susceptibility.

Within the lipid-metabolism module, PUFA-rich phospholipids including PE(20:5/18:4) and PC(O-16:0/20:4) accumulate in serum from SA patients, as validated by quantitative bar-chart data. These PUFA-containing phospholipids may be hydrolysed by phospholipase A2 (PLA2), releasing free eicosapentaenoic acid (EPA) (43). Free PUFA substrates are further catalysed by lipoxygenase (LOX) to produce cytotoxic lipid-peroxide derivatives, including 18-HEPE, 8-HDoHE and 14-Hydroxy-E4-neuroprostane. Accumulation of these oxidized lipid mediators may induce intracellular ROS overload and impair membrane integrity, serving as potential upstream triggers for ferroptosis in trophoblast and decidual cells (44).

Multiple endogenous antioxidant metabolites decline in SA circulation, such as 4-hydroxyestrone-2-S-glutathione, bilirubin and tetrahydrofolic acid, consistent with quantitative observations in the embedded bar graphs. Tetrahydrofolate deficiency may compromise one-carbon and redox metabolism, and thereby potentially affect glutathione-dependent antioxidant capacity (45). Meanwhile, downregulated O-palmitoylcarnitine and succinic acid indicate defective mitochondrial fatty acid uptake and oxidative capacity, potentially resulting in mitochondrial energy exhaustion and aggravating oxidative tissue injury. Collectively, insufficient antioxidant defense may drive lipid peroxidation and subsequent ferroptosis-related metabolic perturbations, which may constitute the core metabolic signature of idiopathic spontaneous abortion. This synergistic metabolic cascade could trigger irreversible damage to decidual and villous trophoblast, ultimately leading to embryonic growth arrest and pregnancy loss (46).

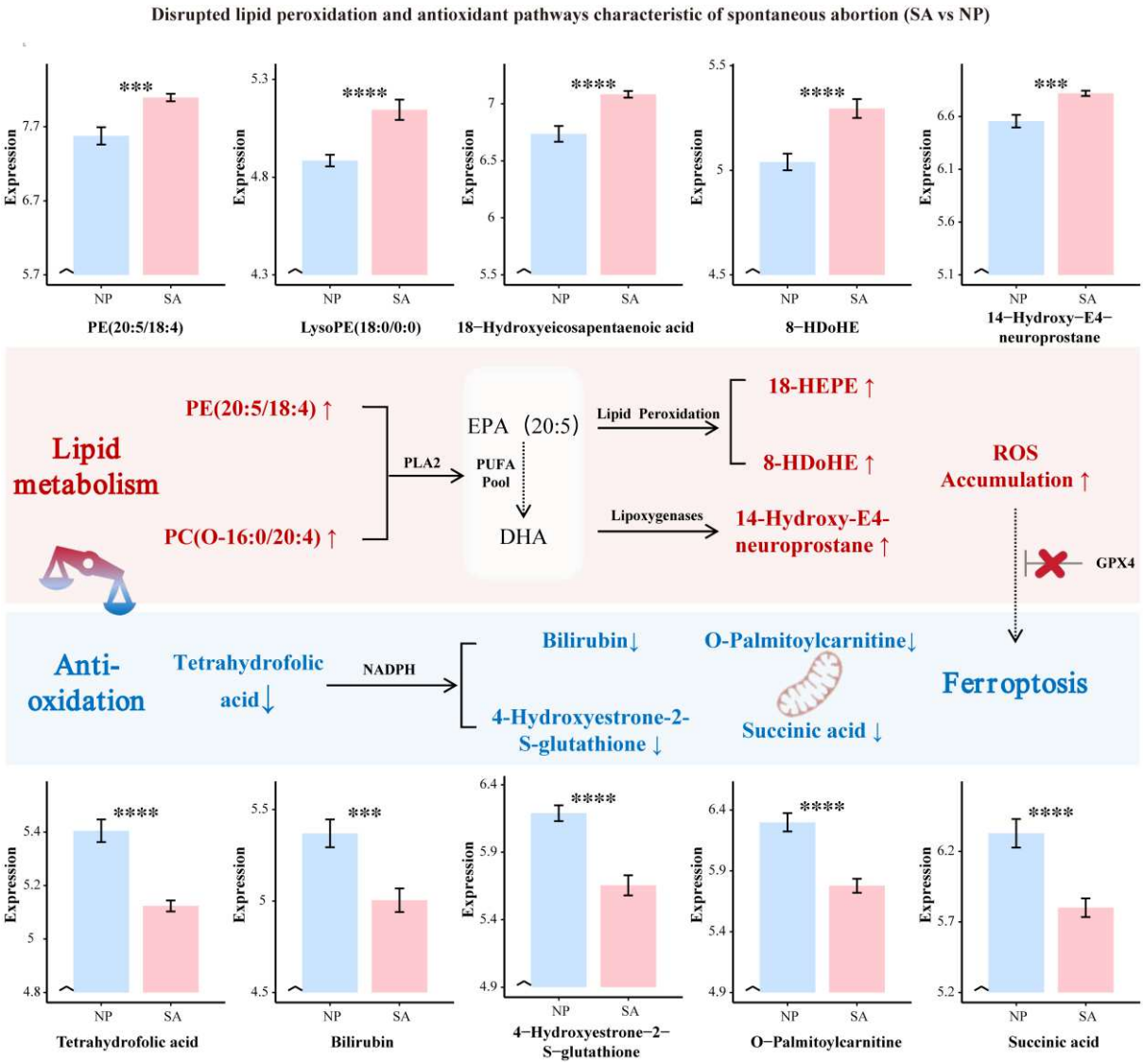


Figure 7. Integrated schematic of ferroptosis and oxidative stress-associated core metabolic pathway dysregulation distinguishing SA from NP.

The central interconnected regulatory network illustrates crosstalk among PUFA lipid-peroxidation cascades, endogenous antioxidant depletion, mitochondrial energy dysfunction, and downstream ferroptosis activation. Upward arrows denote metabolites significantly elevated in SA; downward arrows indicate metabolites depleted in SA. Peripheral bar charts show normalized relative serum expression of core nodal metabolites linked to ferroptosis and antioxidant responses. Values are presented as the mean ± standard error of the mean (SEM). Statistical significance: ***$P < 0.001$, **** $P < 0.0001$.

Single-cell transcriptomic profiling reveals cellular atlas remodelling of decidual microenvironments in NP, SA and TP.

Single-cell RNA sequencing was prospectively performed on first-trimester uterine decidual specimens from TP patients in our centre. The decidua constitutes the critical maternal compartment of the maternal-fetal interface and dominates immune tolerance, stromal

remodelling and vascular adaptation during early gestation; dysregulation of decidual homeostasis is tightly implicated in the occurrence of spontaneous abortion and tubal ectopic pregnancy. Gestational age-matched scRNA-seq datasets of decidual samples from NP and SA cohorts were retrieved from published literatures (PMID: 36355621, 33482359). All datasets were integrated to construct a high-resolution single-cell transcriptional atlas of human first-trimester maternal-fetal interface (Figure 8A). Detailed sample information and sequencing quality metrics of all integrated samples are summarized in Supplementary Table S11. Unsupervised UMAP clustering identified eleven major cell populations residing in the maternal-fetal interface, including decidual stromal cells (DSCs), uterine NK cells (uNK), T cells, macrophages, epithelial cells, neutrophils, B cells, dendritic cells (DCs), endothelial cells, mast cells and perivascular cells. Cell annotation was implemented relying on canonical cell-type-specific marker genes: DSCs were characterized by IGFBP6 and PAEP, endothelial cells by VWF, macrophages by CD68, DCs by *CLEC9A*, uNK cells by *KLRC1*, and T cells by *CD3D*. The UMAP distribution of annotated cell subsets and the expression patterns of signature marker genes are visualized in Figure 8B.

Stacked bar charts were applied to quantify the proportional distribution of all annotated cell subsets across NP, SA and TP cohorts (Figure 8C), and the corresponding absolute cell counts and proportional values of each cell population in different groups are summarized in Supplementary Table S12. Obvious intergroup differences were found in several functionally vital cell populations related to gestational homeostasis: DSCs were markedly less abundant in the SA group relative to the NP and TP groups; macrophage proportions were similar between NP and TP but declined notably in SA; endothelial cells showed a higher proportion in TP than those in NP and SA. Among all cell subsets, DSCs, endothelial cells (ECs), and macrophages exhibited the largest magnitude of abundance alterations across the three cohorts and were therefore selected as core cell populations for subsequent in-depth analysis. On this basis, we further constructed global ligand-receptor interaction networks to characterize intercellular signalling crosstalk within the decidual microenvironment. The overall strength of cell-cell communication across all cell subsets was visualized for NP, TP and SA groups separately (Figure 8D). The results demonstrated that DSCs, macrophages and endothelial cells acted as core signalling hubs with the most abundant ligand-receptor pairs and the strongest intercellular communication activity; characteristic remodelling of signalling intensity among these three cell populations was observed in SA and TP groups. Therefore, subsequent analyses focused on these three pivotal cell subsets to explore their transcriptional reprogramming patterns and

clarify their pathogenic mechanisms that may contribute to decidual homeostatic disturbance in SA and TP.

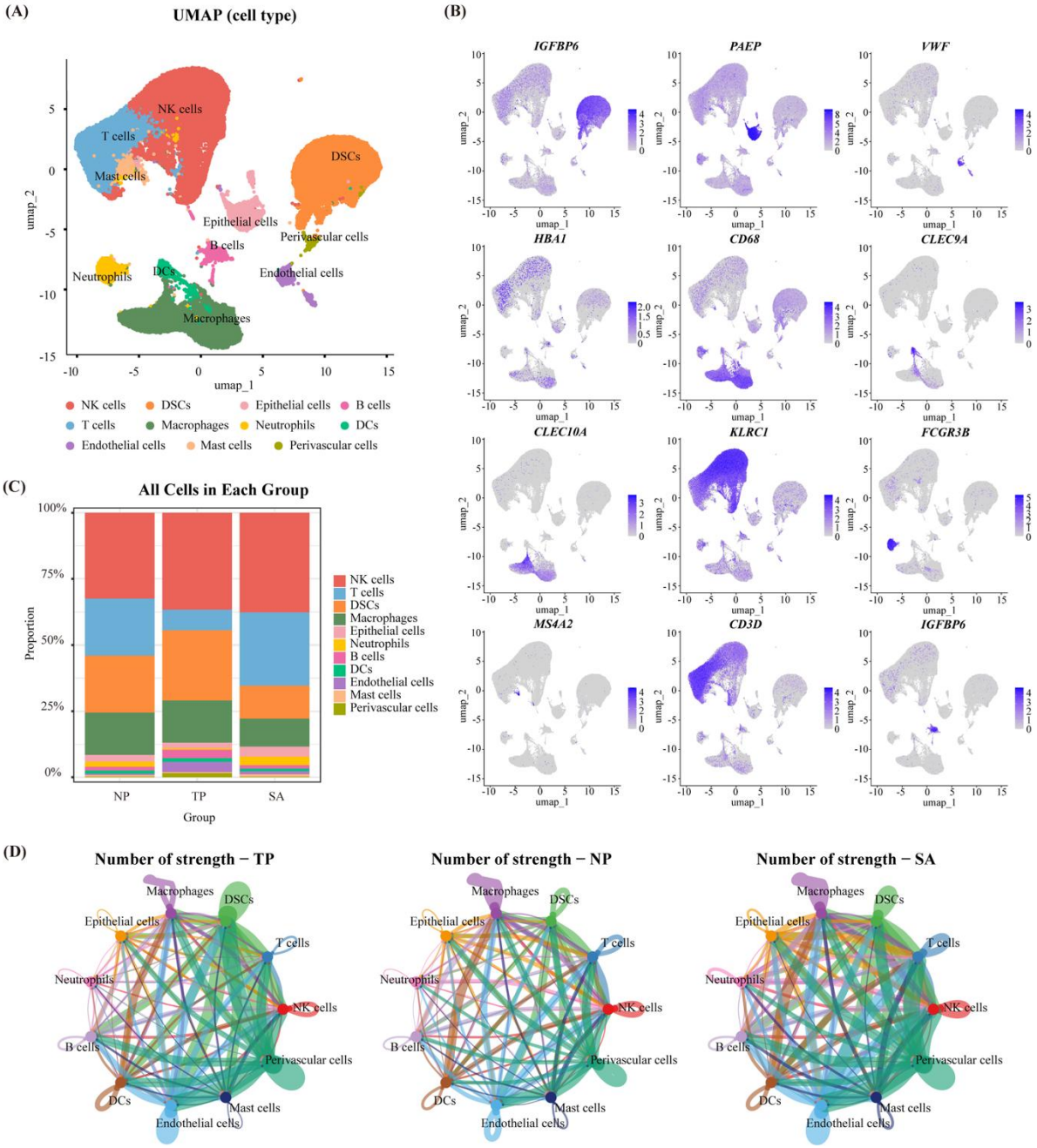


Figure 8. Global single-cell transcriptomic atlas of human first-trimester maternal-fetal interface tissues from NP, SA and TP cohorts.

(A) Integrated UMAP visualization displaying eleven major cell populations identified from merged scRNA-seq datasets of NP, SA and TP decidual samples after batch effect correction by Harmony algorithm.

(B) Feature plots showing the representative canonical marker genes for each annotated cell subtype.

(C) Stacked bar diagram illustrating the relative proportional distribution of all cell subsets in three cohorts; raw cell counts and proportion data are provided in Supplementary Table S12.

(D) Quantification of comprehensive intercellular interaction strength across the global cell communication network.

Shared Lipid Metabolic Reprogramming in Decidual Stromal Cell Subsets Underlying Adverse Pregnancy Outcomes

DSCs act as central regulators of decidual homeostasis and maternal–fetal signal crosstalk. To resolve transcriptional heterogeneity of DSCs under normal and pathological pregnancy states, subclustering analysis was performed on the DSC dataset. Based on Clustree stability evaluation, UMAP re-clustering at a resolution of 0.15 partitioned DSCs into three transcriptionally distinct subpopulations (dsc1, dsc2, dsc3). Split UMAP plots and stacked bar charts further revealed divergent distribution patterns of the three subsets across NP, SA and TP groups (Figure 9A). Dot plots of cluster-specific marker genes together with GO biological process enrichment analyses uncovered disparate functional features of each subcluster (Figure 9B).

The dsc1 subset dominated NP samples and exhibited high transcriptional abundance of canonical decidualization marker *IGFBP1*. This cluster was markedly enriched in pathways related to cytoplasmic translation, oxidative phosphorylation and cellular respiration, consistent with its identity as metabolism-stabilized DSCs sustaining basal energy homeostasis in normal decidua. The dsc2 subset was preferentially enriched in SA decidua. Genes upregulated in dsc2 were mainly implicated in decidual matrix remodelling, angiogenesis and negative immune regulation, demonstrating that dsc2 functions as immunomodulatory DSCs to maintain maternal–fetal immune tolerance and coordinate uterine vascular reconstruction.

A Venn diagram was generated to screen overlapping differentially upregulated genes in dsc2 and dsc3 relative to dsc1; bubble plot enrichment further annotated the biological functions of these shared dysregulated genes (Figure 9C). Violin plots validated that multiple pivotal lipid transport genes (*ABCA1*, *CAV1*, *LDLR*, *PLIN2*) exhibited obvious expression disparities among the three DSC subpopulations, implying intrinsic heterogeneity in lipid metabolism at the single-cell level (Figure 9D). Oil Red O histological staining was implemented to verify in situ intracellular lipid deposition within decidual tissues (Figure 9E). NP decidua contained sparse tiny lipid droplets; TP decidua presented moderate lipid accumulation; SA decidua displayed massive aggregation and fusion of lipid droplets. Semi-quantitative H-score analysis confirmed significantly aggravated lipid deposition in both pathological groups, with the most severe lipid metabolic disturbance observed in SA tissues. Collectively, although SA and TP are characterized by preferential expansion of functionally distinct DSC subsets, both adverse

pregnancy conditions induce conserved lipid metabolic reprogramming in DSCs. Such universal lipid overload within stromal cells triggers excessive intracellular lipid accumulation and cellular functional impairment, which serves as a convergent core pathological feature shared by these two pathological pregnancy phenotypes.

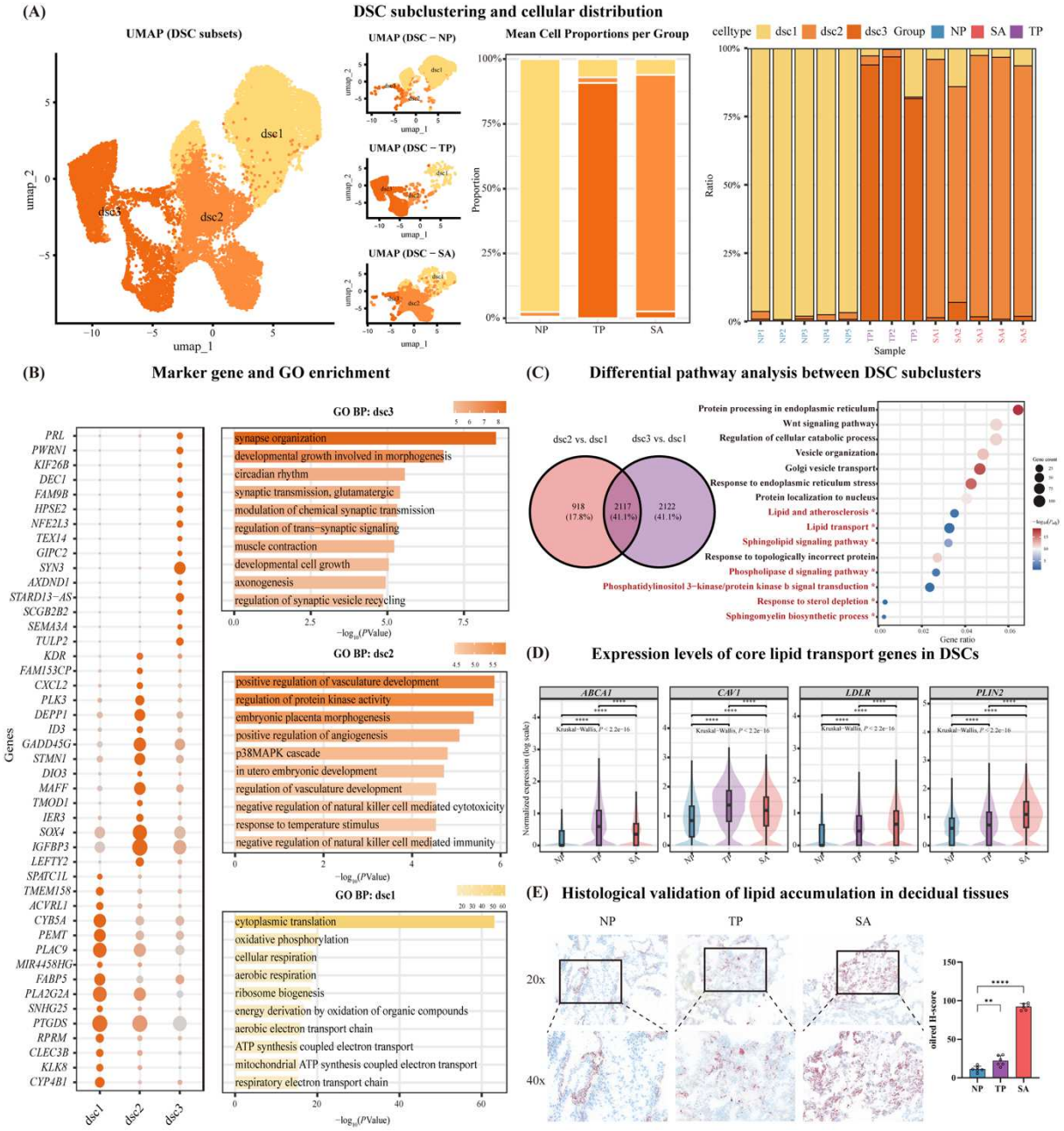


Figure 9. Subclustering, functional annotation and lipid metabolic characteristics of decidual stromal cell subsets from NP, SA and TP cohorts.

(A) UMAP visualization of re-clustered decidual stromal cells showing three transcriptionally distinct DSC subpopulations; group-stratified split UMAP plots and stacked bar charts illustrating the proportional distribution of DSC subsets across NP, SA and TP groups.
(B) Dot plots of subset-specific signature genes and corresponding GO biological process enrichment bar charts for each DSC subcluster.

(C) Venn diagram displaying overlapping upregulated genes in dsc2/dsc3 versus dsc1, and bubble plots showing functional enrichment of shared dysregulated genes.
(D) Violin plots comparing the expression levels of core lipid transport-related genes among three DSC subsets.
(E) Representative Oil Red O staining images and semi-quantitative H-score analysis of intracellular lipid accumulation in NP, SA and TP decidual tissues.

Decidual Endothelial Cell Polarization Drives Distinct Inflammatory and Ferroptosis Signatures in TP and SA

ECs constitute the primary vascular barrier at the maternal–fetal interface and modulate immune cell recruitment toward embryonic implantation sites. Subclustering analysis of decidual ECs resolved three transcriptionally distinct subpopulations: vascular ECs, lymphatic ECs and proliferating ECs. Group-split UMAP visualizations and stacked proportional bar charts revealed evident compositional remodelling of EC subsets across NP, SA and TP cohorts (Figure 10A). CD31 immunofluorescence presented divergent vascular pathological phenotypes in the two pathological pregnancies; uterine decidua from TP patients harboured sparsely distributed and structurally disorganized $CD31^{+}$ blood vessels, while intrauterine decidua from SA exhibited obvious inflammatory activation of vascular endothelium (Figure 10B).

To characterize TP-specific transcriptional reprogramming in decidual endothelium, Z-score-normalized heatmaps were generated to compare core genes of the tricarboxylic acid (TCA) cycle and arachidonic acid-mediated inflammatory cascades between NP and TP ECs (Figure 10C). TP-derived ECs exhibited disrupted intracellular energy homeostasis alongside robust pro-inflammatory signalling hyperactivation. Multiple rate-limiting TCA cycle enzymes (*IDH2, MDH2, OGDH, PDHA1*) and arachidonic acid-derived pro-inflammatory mediators (*ALOX5, LTA4H, PLA2G4A, PTGS2*) were markedly upregulated in TP ECs, collectively forming an endothelium-originated pro-inflammatory metabolic microenvironment under ectopic embryo implantation. Dot plots of signature genes across five functional modules (extracellular matrix mechanics, energy metabolism, lipid metabolism, hypoxia response, inflammatory signalling) were used to compare transcriptional profiles across the three cohorts (Figure 10D). In TP ECs, genes related to energy metabolism (*SLC2A3, PFKFB3, CPT1A*), lipid metabolism (*ACSL4, PLCB1*), hypoxia response (*HIF1A, FOXO1*) and inflammatory signalling (*NFKB1*) showed elevated expression and a higher fraction of positive cells relative to NP controls, with more prominent activation of hypoxia and inflammatory pathways in TP endothelium. Our serum metabolomic findings in Result 3 identified lipid peroxidation and

glutathione depletion as core metabolic features associated with SA. To explore the endothelial basis of this phenotype, we calculated a single-cell ferroptosis susceptibility index and compared NP and SA groups using ridge plots. SA decidual ECs had significantly higher ferroptosis susceptibility index scores than NP ECs (Figure 10E). Spearman correlation analysis demonstrated significant negative correlations between *APOE/PTGDS* expression and ferroptosis susceptibility scores in NP and SA ECs (Figure 10F). This inverse association indicates impaired lipid efflux and compromised endogenous anti-ferroptosis protection in SA endothelial cells, which may promote excessive intracellular lipid peroxidation and microvascular endothelial injury, potentially contributing to early pregnancy loss.

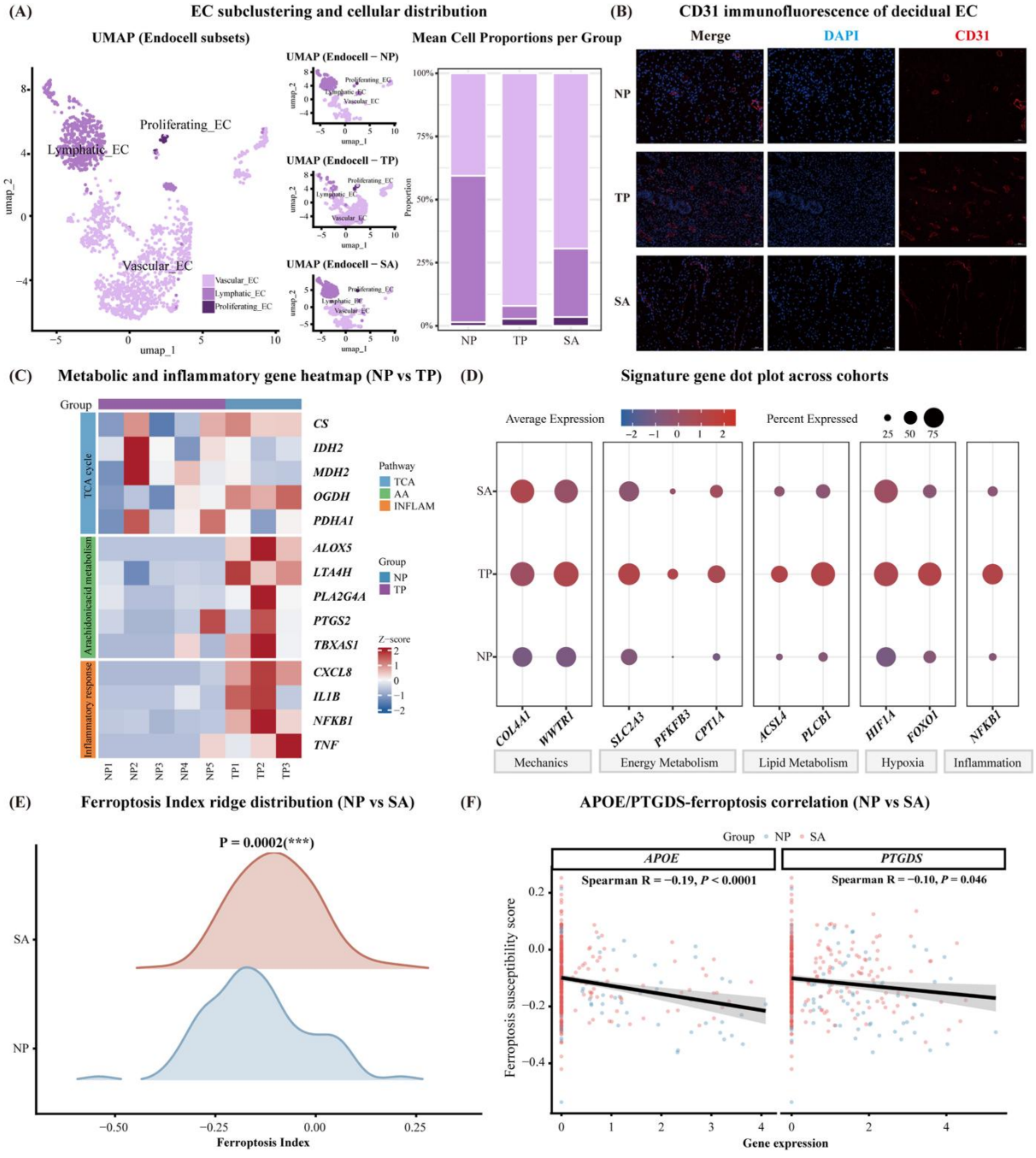


Figure 10. Subclustering and pathological functional analysis of ECs in NP, SA and TP.

(A) UMAP reclustering results of decidual ECs and stacked bar charts quantifying the proportional distribution of EC subpopulations in three groups.
(B) Representative CD31 immunofluorescence staining images of decidual vascular endothelium from NP, SA and TP decidua.
(C) Z-score normalized heatmap illustrating differential expression of core genes involved in TCA cycle metabolism and arachidonic acid-mediated inflammatory response between NP and TP ECs.
(D) Dot plots showing the average expression ratio and positive cell percentage of signature genes assigned to five functional modules among all three cohorts.
(E) Ridge distribution plots comparing the overall ferroptosis susceptibility index of ECs between NP and SA groups.
(F) Spearman correlation analyses between the expression levels of *APOE/PTGDS* and single-cell ferroptosis susceptibility scores in NP and SA ECs.

Macrophage heterogeneity reveals distinct functional states in TP and SA decidua

Decidual macrophages act as central orchestrators of maternal-fetal immune homeostasis. Subclustering of decidual macrophages identified three transcriptionally distinct populations, annotated as Mac1, Mac2 and Mac3 (Figure 11A), whose independent segregation was confirmed by t-SNE. Subset composition differed markedly among groups: NP decidua contained mainly Mac1 and Mac2, SA decidua was dominated by Mac1, and the Mac3 state was selectively expanded in TP (Figure 11A). Cluster-specific marker gene dot plots and GO biological process enrichment delineated specialized functional identities for each macrophage population (Figure 11B).

Mac1 displayed pro-inflammatory, M1-like transcriptional features. Pro-inflammatory module scores differed significantly among groups (Figure 11C): Mac1 cells from SA scored highest, whereas those from TP were suppressed. Given the serum lipid peroxidation signature observed in SA, we next assessed ferroptosis susceptibility in Mac1. The ferroptosis susceptibility index was significantly higher in SA than NP Mac1 cells, with no obvious difference between TP and NP (Figure 11D). Dot plots showed that ferroptosis-associated genes (27) *SLC3A2*, *MAP1LC3B*, *NCOA4*, *VDAC2* and iron-regulatory gene *CP* (47) were upregulated in SA Mac1 macrophages, accompanied by decreased expression of the anti-ferroptotic gene *GPX4* (Figure 11E). These results indicate that enhanced pro-inflammatory transcriptional program within Mac1 macrophages is closely associated with elevated ferroptosis-associated vulnerability under spontaneous abortion conditions.

Beyond confirming subset segregation, t-SNE analysis corroborated the selective enrichment of the Mac3 state in TP decidua (Figure 11F). To explore the metabolic basis of this

TP-specific state, we compared lipid metabolism pathway module scores across the three macrophage subsets. Mac3 showed specifically elevated scores in glycerophospholipid and fatty acid metabolism pathways (Figure 11G), consistent with its tissue-resident immune-regulatory phenotype and the cytoskeleton remodeling and vesicle trafficking functions indicated by GO enrichment analysis. This cellular signature aligned with our serum metabolomic findings in TP, which identified systemic dysregulation of glycerophospholipid metabolism and fatty acid-derived inflammatory lipid signaling; the concordant alteration of glycerophospholipid metabolism at both circulatory and cellular levels provides convergent, cross-level evidence for lipid metabolic reprogramming in TP.

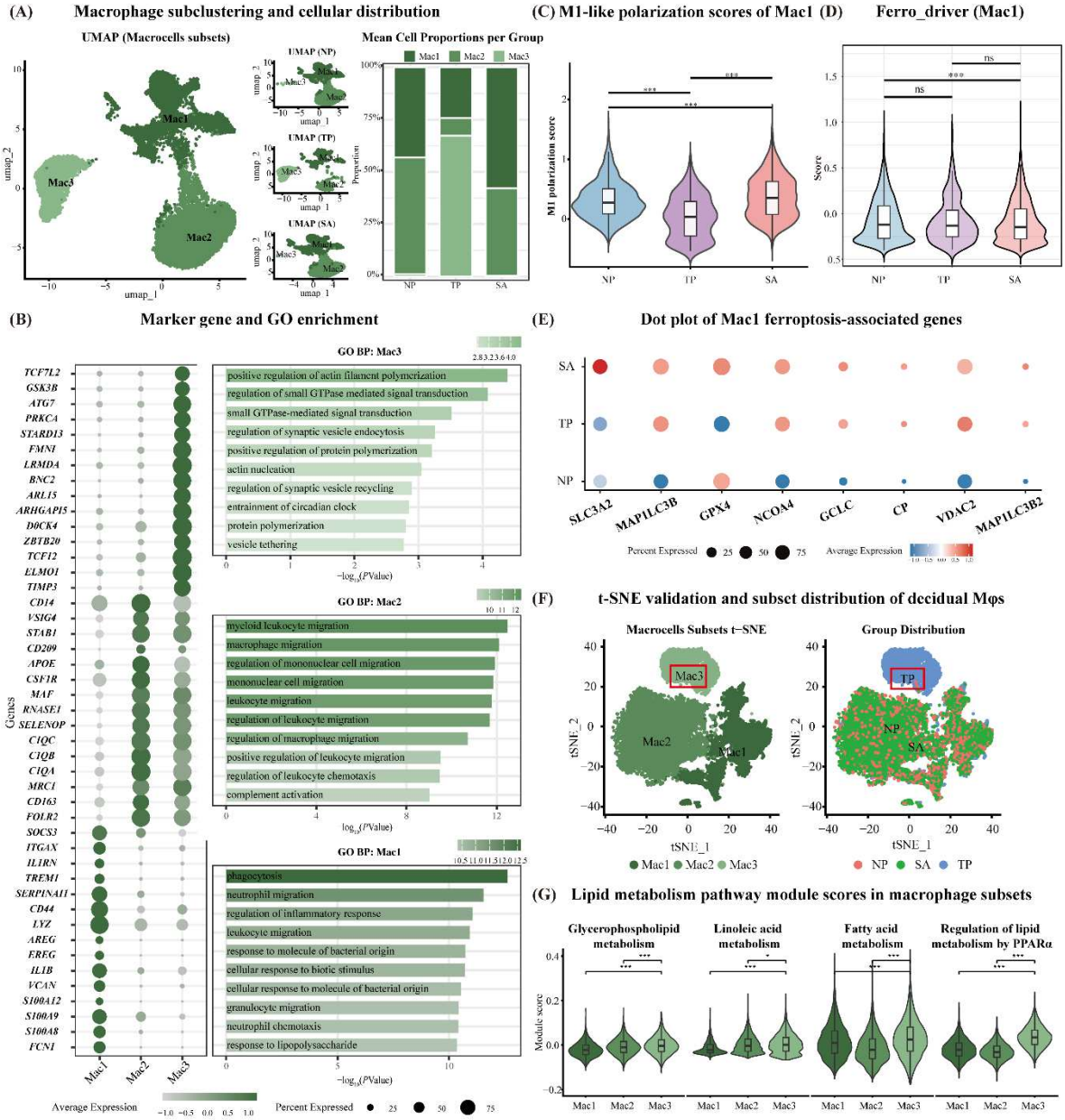


Figure 11. Macrophage subclustering and TP-specific functional features of the Mac3 regulatory macrophage state.

(A) UMAP re-clustering of decidual macrophages into Mac1/Mac2/Mac3 subsets and subgroup cell proportion bar charts.
(B) Dot plots of subset-specific marker genes and GO biological process enrichment bar charts for each macrophage subcluster.
(C) Violin plots showing pro-inflammatory/M1-like transcriptional scores of Mac1 decidual macrophages among the three groups.
(D) Violin plots of ferroptosis susceptibility index values in Mac1 decidual macrophages.
(E) Dot plot showing the expression pattern of representative ferroptosis-associated genes in Mac1 decidual macrophages.
(F) t-SNE validation of macrophage subset segregation and group distribution.
(G) Lipid metabolism pathway module scores across macrophage subsets.

Discussion

This study aimed to profile serum metabolic signatures and identify early serum metabolic biomarkers for adverse early pregnancy outcomes. We also intended to find serum metabolic markers that can spot unfavorable early pregnancy conditions at an early time point. Our analysis scheme was designed to fit the routine tiered diagnostic logic used clinically for early pregnancy cases with unclear clinical diagnosis (19). We first compared patients with TP against the pooled IUP cohort to screen differential metabolic signatures distinguishing ectopic pregnancy from intrauterine gestation. Subsequently, the IUP population was subdivided into NP and SA subgroups to explore metabolites indicative of embryonic developmental prognosis.

TP cases showed enhanced glycerophospholipid degradation compared with IUP controls. This metabolic change was accompanied by activated arachidonic acid signaling and impaired tricarboxylic acid (TCA) cycle function. Increased lysoPC content and higher PLA2 activity promoted the synthesis of multiple pro-inflammatory lipid mediators, including prostaglandin D2 and leukotriene E4. Impaired fatty acid β-oxidation was evident in TP patients, with L-octanoylcarnitine accumulation and decreased acetylcarnitine abundance. Elevated succinate levels further indicated disrupted mitochondrial energy metabolism. These metabolic derangements coincide with the hypoxic microenvironment inherent to tubal ectopic implantation (48), accompanied by excessive synthesis of pro-inflammatory lipids and dysfunctional mitochondrial energy metabolism (49). In contrast to NP, SA patients displayed pronounced lipid peroxidation and widespread redox metabolic disorders related to the ferroptosis pathway. Extensive hydrolysis of polyunsaturated phospholipids generates oxidation-sensitive substrates, which further produce cytotoxic lipid metabolites such as 18-

HEPE and 8-HDoHE. Decreased levels of tetrahydrofolate, bilirubin, succinate, and O-palmitoylcarnitine indicate impaired endogenous antioxidant defense and mitochondrial dysfunction. Persistent systemic oxidative stress derived from such metabolic dysregulation ultimately contributes to embryonic developmental failure (50).

We performed LASSO regularized regression to screen differential metabolic features and evaluated the predictive efficacy of six machine learning models. Among the six algorithms, the LightGBM model delivered the strongest diagnostic performance, yielding AUC values of 0.948 for TP/IUP discrimination and 0.985 for distinguishing viable from non-viable intrauterine pregnancies. The core predictive metabolites for TP were kynurenine and glycerol 3-phosphate (42). Glycerol 3-phosphate has been identified as a signature metabolite of disordered glycolipid metabolism in pathological pregnancy, with abnormal accumulation observed in gestational diabetes mellitus (51). These metabolic alterations are consistent with the inflammatory activation and mitochondrial dysfunction underlying tubal pregnancy. For SA prediction, 3-hydroxyanthranilic acid was identified as the key biomarker closely associated with systemic oxidative stress. Dysregulated kynurenine pathway metabolites, including kynurenine and 3-hydroxykynurenine, have also been reported in pathological pregnancy such as preeclampsia (52). Consistent with our metabolomic results, mildly elevated circulating glutathione was observed in SA patients, which represents an endogenous antioxidant compensatory response triggered by sustained and intense lipid peroxidation stress (53). This paradoxical metabolic alteration has been validated in clinical studies, confirming that miscarriage patients exhibit increased peripheral glutathione levels accompanied by impaired antioxidant enzyme activity, forming a compensatory but functionally defective antioxidant phenotype (54). Such adaptive glutathione upregulation is insufficient to reverse persistent oxidative damage at the maternal-fetal interface and therefore cannot sustain normal early pregnancy progression (55).

Serum metabolic profiling enables molecular discrimination between TP and SA, and machine learning-derived signatures quantify systemic metabolic perturbations to support precise risk stratification for abnormal early pregnancy. However, circulating metabolic data cannot pinpoint the specific decidual cell populations driving systemic metabolic reprogramming. To address this limitation, we integrated high-resolution scRNA-seq profiling of first-trimester decidual specimens to dissect the molecular linkage between peripheral metabolic disorders and maternal-fetal interface pathology. ScRNA-seq analysis of NP, TP and SA decidual samples profiled key cellular components, including DSCs, endothelial cells,

macrophages. DSCs from both TP and SA decidua exhibited prominent intracellular lipid accumulation, which was further confirmed by Oil Red O staining. Lipid accumulation of this kind within pathological decidual tissue constitutes the core cellular basis of systemic lipid metabolic disorders in these two pregnancy complications. The unique hypoxic microenvironment of tubal pregnancy remodels the TP decidual immune landscape: it enriches immunoregulatory Mac3 macrophages and restricts pro-inflammatory activation of Mac1 macrophages. TP decidual endothelial cells also upregulated genes associated with TCA cycle metabolism and arachidonic acid-mediated inflammation. These cellular alterations recapitulate the systemic inflammatory and mitochondrial metabolic dysfunction observed in serum metabolomics. In contrast, SA decidua is dominated by pro-inflammatory Mac1 macrophage polarization. Single-cell analysis revealed that SA decidual endothelial cells and Mac1 macrophages present a ferroptosis-related transcriptional signature characterized by elevated ferroptosis susceptibility and reduced *GPX4* expression. This cell-type-specific redox dysregulation correlates with peripheral systemic lipid peroxidation, rather than directly driving terminal pregnancy injury(Figure 12).

This study integrates metabolomics, machine learning and single-cell transcriptomics to characterize distinct lipid, energy and redox dysregulations in TP and SA, and clarify the correlational linkage between decidual cell dysfunction and systemic metabolic disorders. The screened biomarkers enable precise pregnancy classification and embryonic status evaluation, providing an effective early warning strategy for abnormal early pregnancy. This study has limitations of single-center enrollment and limited sample size, and the LightGBM classifier lacks external multi-center validation. All multi-omic findings are correlational, and additional functional experiments will be required to verify the causal mechanisms that connect metabolic dysregulation with adverse pregnancy outcomes. Future multi-center prospective studies will validate the stability and generalizability of these metabolic signatures.

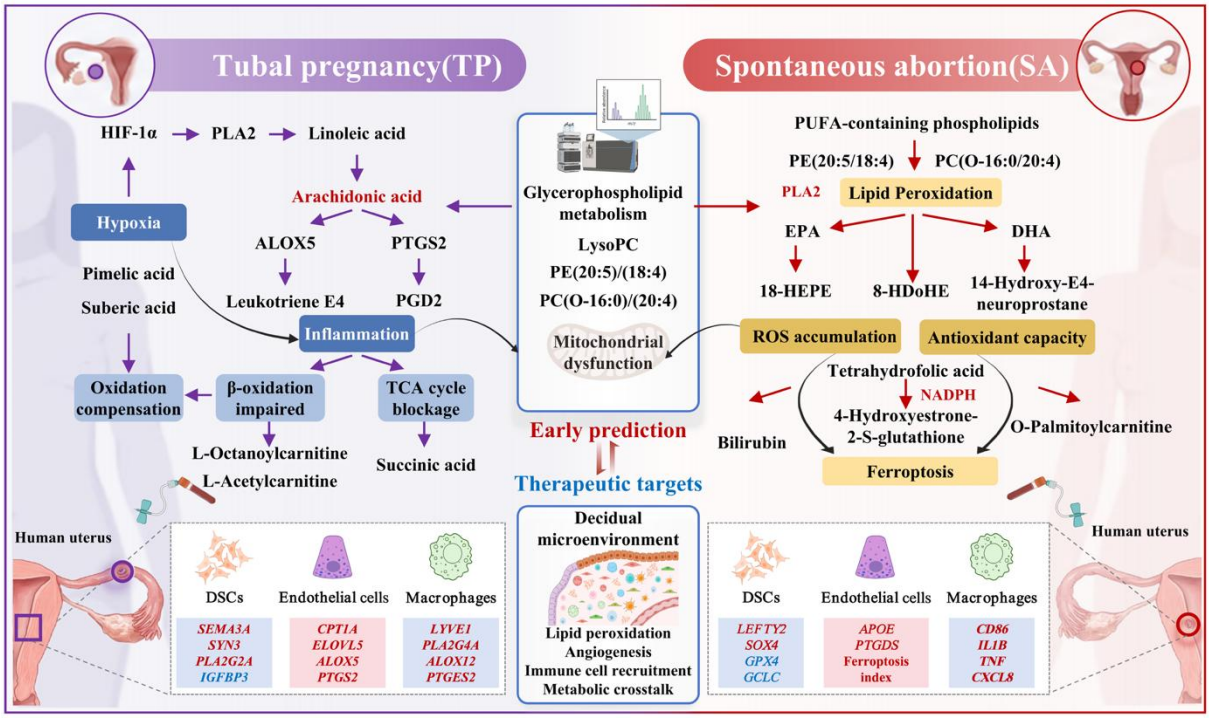


Figure 12. Schematic summary of metabolic and cellular alterations in tubal pregnancy and spontaneous abortion.

Conclusion

This study integrated serum metabolomics and decidual single-cell transcriptomics to elucidate distinct metabolic pathogenic mechanisms underlying TP and SA. Both early pregnancy complications exhibit upregulated glycerophospholipid metabolism, representing a shared upstream metabolic perturbation. TP is characterized by TCA cycle dysfunction and decidual inflammatory activation, whereas SA manifests disturbed glutathione-related redox metabolism, impaired antioxidant capacity and sustained lipid peroxidation that triggers decidual ferroptosis. Based on the identified metabolic signatures, we established a two-stage machine learning model with favorable diagnostic performance, achieving an AUC of 0.948 for pregnancy location discrimination and 0.985 for embryonic viability evaluation. Single-cell transcriptomic profiling further links circulating metabolic dysregulation to cell-type-specific decidual damage in pathological pregnancies. Future multicenter prospective cohorts are required to validate the generalizability of these metabolite biomarkers. The disease-specific metabolic regulators identified in this work may offer preliminary clues for the stratified intervention of heterogeneous early pregnancy disorders.

Abbreviations

AUC Area Under the Receiver Operating Characteristic Curve
BMI Body Mass Index
BCR B Cell Receptor
Cer Ceramides
DC Dendritic Cell
DEG Differentially Expressed Gene
DG Diradylglycerolipids
DSC Decidual Stromal Cell
DT Decision Tree
EC Endothelial Cell
FA Fatty Acids
FDR False Discovery Rate
GO Gene Ontology
IQR Interquartile Range
IUP Intrauterine Pregnancy
GSH Glutathione
KEGG Kyoto Encyclopedia of Genes and Genomes
LASSO Least Absolute Shrinkage and Selection Operator
LC-MS Liquid Chromatography–Mass Spectrometry
LCL Lyso-glycerophosphocholines
LPE Lyso-glycerophosphoethanolamines
LightGBM Light Gradient Boosting Machine
MG Monoradylglycerolipids
MLP Multi-Layer Perceptron
mTORC1 Mammalian Target of Rapamycin Complex 1
NES Normalized Enrichment Score
NP Normal Intrauterine Pregnancy
OPLS-DA Orthogonal Partial Least Squares-Discriminant Analysis
PA Glycerophosphates
PCA Principal Component Analysis
PC Glycerophosphocholines
PCoA Principal Coordinate Analysis
PDW Platelet Distribution Width
PERMANOVA Permutational Multivariate Analysis of Variance
PE Glycerophosphoethanolamines
PG Glycerophosphoglycerols
PI Glycerophosphoinositols
PLS-DA Partial Least Squares-Discriminant Analysis
PR-AUC Area Under the Precision-Recall Curve
PUL Pregnancy of Unknown Location
PUFA Polyunsaturated Fatty Acid
QC Quality Control
ROC Receiver Operating Characteristic
RF Random Forest
RSVM Radial-Basis Support Vector Machine
SA Spontaneous Abortion
scRNA-seq Single-Cell RNA Sequencing

SEM Standard Error of the Mean
SHAP SHapley Additive exPlanations
SM Sphingomyelins
t-SNE t-Distributed Stochastic Neighbor Embedding
TCA Tricarboxylic Acid Cycle
TG Triradylglycerolipids
TP Tubal Ectopic Pregnancy
TVUS Transvaginal Ultrasonography
UHPLC-MS/MS Ultra-High-Performance Liquid Chromatography-Tandem Mass Spectrometry
UMAP Uniform Manifold Approximation and Projection
VIP Variable Importance in Projection
XGBoost Extreme Gradient Boosting
β-hCG β-human Chorionic Gonadotropin

Acknowledgements

We gratefully acknowledge all patients diagnosed with tubal ectopic pregnancy, spontaneous abortion, and normal intrauterine pregnancy who actively participated in this research and generously donated clinical serum specimens and decidual tissues for our study. We appreciate the technical staff at the mass spectrometry platform for supporting untargeted metabolomic detection and the laboratory team assisting with single-cell RNA sequencing data processing. We also acknowledge all clinicians in the Department of Gynecology who assisted in clinical sample collection and clinical data collation.

Author contributions

L.H. and Y.Y. jointly put forward the research idea and formulated the overall study design. Multiple authors including Y.H., L.Y., X.L., X.W., X.R.K.L., J.H., X.H., Y.L. and Z.L. participated in clinical specimen collection and systematic sorting of baseline clinical information. L.H. independently completed UHPLC-MS/MS metabolomic profiling and corresponding multivariate statistical data analysis. K.L. and Z.L. were responsible for the bioinformatics interpretation and data processing of single-cell RNA sequencing results. Model construction of machine learning-based diagnosis and SHAP interpretability analysis were accomplished by L.H. The first version of the manuscript was drafted by L.H. and Y.Y. Y.Z. took charge of the daily management and quality control of the clinical cohort enrolled in this study. J.G. and Z.Liu undertook overall supervision of the whole research program, conducted manuscript modification and polishing, and secured the financial support for this project. Every co-author has carefully checked and fully recognized the final manuscript for formal submission.

Funding

The research findings presented in this study were supported by the Key Program of Joint Fund of the National Natural Science Foundation of China (Grant No. U24A20781), as well as the

Clinical Cooperation Project of Integrated Traditional Chinese and Western Medicine for Major Refractory Diseases (Grant No. ZDYN-2024-A-073). All relevant financial resources facilitated the implementation of research design, experimental testing, data analysis and manuscript completion of this study.

Availability of data and materials

The publicly available single-cell datasets of normal pregnancy and spontaneous abortion decidua integrated in our analysis were retrieved from previously published studies: the National Omics Data Encyclopedia (NODE) under accession OEP002901(24), and the Genome Sequence Archive (GSA) under accession HRA000237 (BioProject PRJCA003061)(25). The original single-cell transcriptomic data of uterine decidua tissues with tubal pregnancy obtained from our independent experiments and the serum metabolomic datasets generated in this study can be provided by the corresponding authors upon valid and reasonable academic requests.

Declarations

Ethics approval and consent to participate

The entire research protocol of this project has passed the ethical examination and formal approval by the Ethics Committee of The First Affiliated Hospital of Guangzhou University of Chinese Medicine (Ethics Approval No. JY2025-057). All experimental operations and clinical research procedures strictly followed the ethical principles stipulated in the Declaration of Helsinki. All subjects recruited in this research signed written informed consent documents prior to specimen collection. In addition, all collected clinical specimens and personal patient information were completely de-identified to guarantee the confidentiality of patient privacy.

Consent for publication

All participants enrolled in this research have completed written authorization, allowing the public release of relevant clinical data and overall research outcomes generated in this project.

Competing interests

The research team confirms that there are no potential financial or non-financial conflicting interests associated with the completion and publication of this study.

References

1. Li W, Shen WF, Gu YL, Tao SP, Wei DH, Gao LH. The epidemiology of ectopic pregnancy: global burden and projections. Int J Surg. 2026.

2. Quenby S, Gallos ID, Dhillon-Smith RK, Podesek M, Stephenson MD, Fisher J, et al. Miscarriage matters: the epidemiological, physical, psychological, and economic costs of early pregnancy loss. Lancet. 2021;397(10285):1658-67.

3. Papageorgiou D, Sapantzoglou I, Prokopakis I, Zachariou E. Tubal Ectopic Pregnancy: From Diagnosis to Treatment. Biomedicines. 2025;13(6).

4. Tong F, Wang Y, Gao Q, Zhao Y, Zhang X, Li B, Wang X. The epidemiology of pregnancy loss: global burden, variable risk factors, and predictions. Hum Reprod. 2024;39(4):834-48.

5. Doubilet PM, Benson CB, Bourne T, Blaivas M, Society of Radiologists in Ultrasound Multispecialty Panel on Early First Trimester Diagnosis of M, Exclusion of a Viable Intrauterine P. Diagnostic criteria for nonviable pregnancy early in the first trimester. Ultrasound Q. 2014;30(1):3-9.

6. Po L, Thomas J, Mills K, Zakhari A, Tulandi T, Shuman M, Page A. Guideline No. 414: Management of Pregnancy of Unknown Location and Tubal and Nontubal Ectopic Pregnancies. J Obstet Gynaecol Can. 2021;43(5):614-30 e1.

7. Matenchuk BA, Rosychuk RJ, Rowe BH, Metcalfe A, Chari R, Crawford S, et al. Emergency Department Visits During Pregnancy. Ann Emerg Med. 2023;81(2):197-208.

8. Webster K, Eadon H, Fishburn S, Kumar G, Guideline C. Ectopic pregnancy and miscarriage: diagnosis and initial management: summary of updated NICE guidance. BMJ. 2019;367:l6283.

9. Barnhart KT, Fay CA, Suescum M, Sammel MD, Appleby D, Shaunik A, Dean AJ. Clinical factors affecting the accuracy of ultrasonography in symptomatic first-trimester pregnancy. Obstet Gynecol. 2011;117(2 Pt 1):299-306.

10. Du X, Chen Q, Lu M, Hu J, Chen C, Huang K, et al. An individualized risk prediction tool for ectopic pregnancy within the first 10 weeks of gestation based on machine learning algorithms. Front Med (Lausanne). 2025;12:1726606.

11. Bobdiwala S, Saso S, Verbakel JY, Al-Memar M, Van Calster B, Timmerman D, Bourne T. Diagnostic protocols for the management of pregnancy of unknown location: a systematic review and meta-analysis. BJOG. 2019;126(2):190-8.

12. Turkoglu O, Citil A, Katar C, Mert I, Quinn RA, Bahado-Singh RO, Graham SF. Untargeted Metabolomic Biomarker Discovery for the Detection of Ectopic Pregnancy. Int J Mol Sci. 2024;25(19).

13. Ku CW, Tan YB, Chew KY, Ku CO, Ng STC, Tan TC, Lee YH. Untargeted metabolomics reveals key pathways in miscarriage: steroid, folate, fatty acid & glycosaminoglycan metabolism. NPJ Womens Health. 2025;3(1):35.

14. Grieger JA, Bianco-Miotto T, Grzeskowiak LE, Leemaqz SY, Poston L, McCowan LM, et al. Metabolic syndrome in pregnancy and risk for adverse pregnancy outcomes: A prospective cohort of nulliparous women. PLoS Med. 2018;15(12):e1002710.

15. Wang J, Jiang Y, Lv H, Pi D, Han X, Xu B, et al. Metabolic Signature of Gestational Diabetes Mellitus and Risk of Adverse Birth Outcomes: A Prospective Birth Cohort Study. Diabetes. 2026;75(4):726-37.

16. Chen L, Mir SA, Bendt AK, Chua EWL, Narasimhan K, Tan KM, et al. Plasma lipidomic profiling reveals metabolic adaptations to pregnancy and signatures of cardiometabolic risk: a preconception and longitudinal cohort study. BMC Med. 2023;21(1):53.

17. Jung Y, Lee SM, Lee J, Kim Y, Lee W, Koo JN, et al. Metabolomic profiling reveals early biomarkers of gestational diabetes mellitus and associated hepatic steatosis. Cardiovasc Diabetol. 2025;24(1):125.

18. Shi Y, Li K, Ding R, Li X, Cheng Z, Liu J, et al. Untargeted metabolomics and machine learning unveil the exposome and metabolism linked with the risk of early pregnancy loss. J Hazard Mater. 2025;488:137362.

19. Hill CJ, Phelan MM, Dutton PJ, Busuulwa P, Maclean A, Davison AS, et al. Diagnostic utility of clinicodemographic, biochemical and metabolite variables to identify viable pregnancies in a symptomatic cohort during early gestation. Sci Rep. 2024;14(1):11172.

20. Wu Y, Yu X, Li M, Zhu J, Yue J, Wang Y, et al. Risk prediction model based on machine learning for predicting miscarriage among pregnant patients with immune abnormalities. Front Pharmacol. 2024;15:1366529.

21. Liu Y, Fan X, Pang H, Liu S, Wang B, Wang C, et al. Metabolomics Identifies a Panel of Diagnostic Biomarkers for Early Human Embryonic Development Arrest. J Proteome Res. 2023;22(4):1280-6.

22. Vento-Tormo R, Efremova M, Botting RA, Turco MY, Vento-Tormo M, Meyer KB, et al. Single-cell reconstruction of the early maternal-fetal interface in humans. Nature. 2018;563(7731):347-53.

23. Jia Z, Wei Y, Zhang Y, Song K, Yuan J. Metabolic reprogramming and heterogeneity during the decidualization process of endometrial stromal cells. Cell Commun Signal. 2024;22(1):385.

24. Bao S, Chen Z, Qin D, Xu H, Deng X, Zhang R, et al. Single-cell profiling reveals mechanisms of uncontrolled inflammation and glycolysis in decidual stromal cell subtypes in recurrent miscarriage. Hum Reprod. 2023;38(1):57-74.

25. Wang F, Jia W, Fan M, Shao X, Li Z, Liu Y, et al. Single-cell Immune Landscape of Human Recurrent Miscarriage. Genomics Proteomics Bioinformatics. 2021;19(2):208-22.

26. RPL EGGo, Bender Atik R, Christiansen OB, Elson J, Kolte AM, Lewis S, et al. ESHRE guideline: recurrent pregnancy loss: an update in 2022. Hum Reprod Open. 2023;2023(1):hoad002.

27. Zeng Y, Gan J, Cheng J, Wei C, Zhu X, Wei S, Pang L. Identification of important genes related to ferroptosis in early missed abortion based on WGCNA. Sci Rep. 2025;15(1):715.

28. Yao Y, Xu XH, Jin L. Macrophage Polarization in Physiological and Pathological Pregnancy. Front Immunol. 2019;10:792.

29. Gao H, Ma HJ, Li YJ, Li Y, Zhang JR. Relationship between platelet activation markers and spontaneous abortion: A meta-analysis. Open Life Sci. 2022;17(1):1669-78.

30. Dundar O, Pektas MK, Bodur S, Bakir LV, Cetin A. Recurrent pregnancy loss is associated with increased red cell distribution width and platelet distribution width. J Obstet Gynaecol Res. 2015;41(4):551-8.

31. Karadag SN, Korucu DG. The Role of the Delta Neutrophil Index, Pan-Immune Inflammation Value and Other Hematologic Inflammatory Parameters in the Preliminary Diagnosis of Tubal Ectopic Pregnancy. Immun Inflamm Dis. 2026;14(2):e70349.

32. Turkoglu O, Citil A, Katar C, Mert I, Kumar P, Yilmaz A, et al. Metabolomic identification of novel diagnostic biomarkers in ectopic pregnancy. Metabolomics. 2019;15(11):143.

33. Horne AW, Critchley HO. Mechanisms of disease: the endocrinology of ectopic pregnancy. Expert Rev Mol Med. 2012;14:e7.

34. Lai Y, Zhang Y, Zhang H, Chen Z, Zeng L, Deng G, et al. Modified Shoutai Pill inhibited ferroptosis to alleviate recurrent pregnancy loss. J Ethnopharmacol. 2024;319(Pt 2):117028.

35. Shi Y, Xu D. Platelet distribution width and the risk of unexplained recurrent pregnancy loss: a meta-analysis. J Assist Reprod Genet. 2023;40(7):1523-31.

36. American College of O, Gynecologists' Committee on Practice B-G. ACOG Practice Bulletin No. 193: Tubal Ectopic Pregnancy. Obstet Gynecol. 2018;131(3):e91-e103.

37. Karahoda R, Walker D, Abad C, Anandam KY, Murthi P, Staud F. The placental tryptophan pathway across gestation: implications for pregnancy outcomes. Hum Reprod Update. 2026;32(3):356-79.

38. Gendrot B, Vaillancourt C, Fouquet G. Tryptophan's Journey Through Pregnancy: The Role of Serotonin. Int J Tryptophan Res. 2026;19:11786469261449491.

39. Du C, Wang Z, Dai T, Yuan Y, Zhao J, Tuo Y. LncPVT1 modulates decidualization and links to recurrent spontaneous abortions via glucose and lipid metabolic regulation. Sci Rep. 2026;16(1).

40. Nan WH, Qin XS, Li R. Lipid metabolism imbalance: potential pathological mechanism and new intervention ideas for recurrent miscarriage. Yi Chuan. 2025;47(9):979-91.

41. Kuang M, Fu F, Kuang M, Yu X. The metabolism of arachidonic acid and diseases during pregnancy. J Reprod Immunol. 2026;175:104889.

42. Sarikaya S, Sengul-Bag F, Ovali F, Sak F, Aytan-Tomas P, Gunenc O, Vatansev H. Kynurenine pathway activation in ectopic pregnancy: diagnostic value of 3-hydroxykynurenine and 3-hydroxyanthranilic acid; a prospective study. Scand J Clin Lab Invest. 2026;86(2):166-80.

43. Beharier O, Tyurin VA, Goff JP, Guerrero-Santoro J, Kajiwara K, Chu T, et al. PLA2G6 guards placental trophoblasts against ferroptotic injury. Proc Natl Acad Sci U S A. 2020;117(44):27319-28.

44. Chen Y, Zhao X, Gan B, Jin L, Wei J, Yan J. Metabolomics and proteomics analyses reveal the role of the glycerophospholipid metabolism pathway in unexplained recurrent spontaneous abortion. PeerJ. 2025;13:e19317.

45. Socha MW, Flis W, Wartega M. Epigenetic Genome Modifications during Pregnancy: The Impact of Essential Nutritional Supplements on DNA Methylation. Nutrients. 2024;16(5).

46. Zhao X, Guo Z, Zhao S, Wan D, Xu J, Xu Y, et al. Metabolomic Impact of Maternal Barium Exposure on Miscarriage Risk: Identification of Metabolic Biomarkers and Construction of a Risk Prediction Model. Toxics. 2025;13(12).

47. Davalieva K, Bozhinovski G, Kiprijanovska S, Kubelka-Sabit K, Plaseska-Karanfilska D. Proteomics Analysis of Human Chorionic Villi Reveals Dysregulated Pathways That Contribute to Recurrent Pregnancy Loss. Proteomics Clin Appl. 2024;18(6):e202400020.

48. Xu S, Zhang N, Wang Y, Bi X, Wang Y, Wang X, et al. The immunological paradox of tubal ectopic pregnancy: unraveling immune tolerance amidst inflammation via single-cell sequencing. BMC Pregnancy Childbirth. 2025;25(1):1045.

49. Ye Q, Zeng X, Cai S, Qiao S, Zeng X. Mechanisms of lipid metabolism in uterine receptivity and embryo development. Trends Endocrinol Metab. 2021;32(12):1015-30.

50. Chen J, Yin T, Hu X, Chang L, Sang Y, Xu L, et al. CD36-mediated arachidonic acid influx from decidual stromal cells increases inflammatory macrophages in miscarriage. Cell Rep. 2024;43(11):114881.

51. Yu W, Tang K, An R, Ma S, Tan H, Chen M. Study on Association Between Gut Microbiota, Serum Metabolism and Gestational Diabetes Mellitus Based on Metagenomic and Metabolomics Analysis. Nutrients. 2026;18(3).

52. Broekhuizen M, Allenberg H, van der Ley CP, van Zundert SKM, Cai Z, van Faassen M, et al. Pregnancy complications affect kynurenine pathway metabolite concentrations in umbilical cord blood. Reprod Biol Endocrinol. 2025;23(1):105.

53. Biri A, Kavutcu M, Bozkurt N, Devrim E, Nurlu N, Durak I. Investigation of free radical scavenging enzyme activities and lipid peroxidation in human placental tissues with miscarriage. J Soc Gynecol Investig. 2006;13(5):384-8.

54. Duntas LH. Selenium and at-risk pregnancy: challenges and controversies. Thyroid Res. 2020;13:16.

55. Chen Z, Yin H, Long Y, Zhu H, Xiong R, Duan X, et al. Metabonomics analysis of decidual tissue in patients with recurrent spontaneous abortion. J Reprod Immunol. 2025;167:104398.

Supplementary Files

This is a list of supplementary files associated with this preprint. Click to download.

- SupplementaryMaterials.docx
- SupplementaryTable.xlsx